REVIEW

ADVANCED
ENERGY & SUSTAINABILITY
RESEARCH
Open Access

www.advenergysustres.com

Two-Dimensional Metal–Organic Frameworks-Based Electrocatalysts for Oxygen Evolution and Oxygen Reduction Reactions

Qianglong Qi, Jue Hu,* Yingjie Zhang, Wei Li, Bolong Huang,* and Chengxu Zhang*

Due to unique intrinsic properties and flexible structure modulations, 2D metal–organic frameworks (MOFs)-based materials have become the most promising candidates in the electrocatalysts of energy-conversion systems such as oxygen evolution reaction (OER) and oxygen reduction reaction (ORR). Herein, the background of fundamental 2D MOFs is first introduced and 2D MOF-based electrocatalysts are classified based on OER and ORR. Meanwhile, the recent advances in the 2D MOF-based OER and ORR electrocatalysts are emphasized and discussed including the subtle synthesis strategy, novel structures, unique morphologies, superior electrocatalytic performances, and the underlying reaction mechanism. Finally, the challenges and future perspectives for the developments and research of 2D MOFs-based OER and ORR electrocatalysts are proposed.

1. Introduction

In recent years, 2D materials have become the research focus due to their broad applications that originated from their modulable physical and chemical properties.[1] A variety of 2D materials, including graphene,[2] graphdiyne,[3] graphene oxide,[4] metal chalcogenides,[5] carbon nitride,[6] metal oxide,[7] boron nitride,[8] polyphthalocyanine,[9] and porphyrin-based nanomaterials,[10] have been investigated. In particular, the synthesis of 2D metal–organic frameworks (MOFs) has received intense attention due to several advantages including the high surface area, regular pores, and unsaturated open sites.[11] The 2D MOFs have the properties of other 2D materials, such as ductility, permeability, and conductivity, and have been extensively studied for potential applications in gas storage/separations, sensing, and catalysis.[12] The tunable ligand fields around the isolated metal–ion (or cluster) centers in MOFs mean that the catalytic active sites can be well defined as in homogeneous molecular catalysts (albeit with possible crystalline defects), yet the high active site density and durability could be like those of heterogeneous catalysts.[13]

It is worth pointing out that MOFs can form not only a 2D layered structure but also a 3D structure. However, the most reported MOF derivatives were obtained by the pyrolysis treatment of bulk or so-called 3D MOFs at high temperatures. These materials show high potential to form the aggregation, leading to the loss of exposed active sites and the hindering of mass transfer in electrocatalysis.[14] Compared with 3D MOFs, 2D MOFs are better than 3D MOFs in electrocatalysis in terms of active sites, mass transfer, and electron transport. In addition, the adequately exfoliated single layers of 2D MOFs will make each active site on its surface available to substrates and reagents.[11c] Compared with inorganic 2D nanomaterials such as graphene, 2D MOFs materials not only have the properties of inorganic 2D materials but also have mild synthesis conditions. Their chemical and electronic structures can be easily adjusted through the design of the monomer structure, and they are more flexible in structure design and property regulation. Moreover, there are a variety of organic ligands, which result in the unique physical and chemical properties of 2D MOFs. Therefore, the preparation and application of 2D MOFs have become a research hotspot.

Oxygen evolution reaction (OER) and oxygen reduction reaction (ORR) are the two essential reactions in energy-converting and storage systems such as fuel cells, metal–air batteries, and electrochemical water splitting.[15] Currently, noble metal-based catalysts are considered to be the benchmark catalysts, for instance, IrO_2 or RuO_2 for OER and Pt-based catalysts for

Q. Qi, Prof. J. Hu, Prof. W. Li
Faculty of Science
Kunming University of Science and Technology
Kunming 650093, China
E-mail: hujue@kust.edu.cn

Prof. Y. Zhang, Prof. C. Zhang
The Engineering Laboratory of Advanced Battery and Materials of Yunnan Province
Faculty of Metallurgical and Energy Engineering
Kunming University of Science and Technology
Kunming 650093, China
E-mail: chxzhang@kust.edu.cn

Prof. B. Huang
Department of Applied Biology and Chemical Technology
The Hong Kong Polytechnic University
Hung Hom, Kowloon, Hong Kong SAR 999077, China
E-mail: bhuang@polyu.edu.hk

The ORCID identification number(s) for the author(s) of this article can be found under https://doi.org/10.1002/aesr.202000067.

**ADVANCED
SCIENCE NEWS**

www.advancedsciencenews.com

**ADVANCED
ENERGY & SUSTAINABILITY
RESEARCH**
Open Access

www.advenergysustres.com
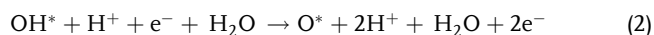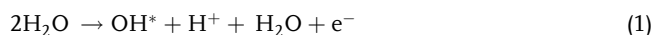
ORR, but their high cost, easy poisoning, and limited abundance hinder their wide application.[16] The development of efficient and stable non-noble metal electrocatalysts is crucial for the commercialization of fuel cells.[17] Because most 2D MOFs are synthesized by inexpensive first-row transition metals (Fe, Co, Ni, etc.) with organic ligands, which display high surface areas and tunable structures, 2D MOFs and their derivatives have become promising electrocatalyst candidates.
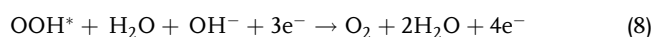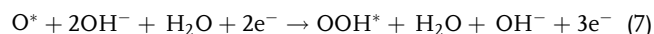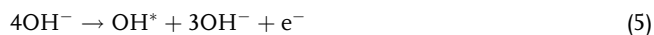
2. 2D MOFs for OER

The OER process involves a four-electron transfer process, which usually requires a large overpotential to deliver the desired current. In the acidic and alkaline environment, the reaction mechanisms are different, which are related to the binding strength of H* and OH, respectively. However, in general, the conversion from O* to *OOH has been reported as the rate-determining step (RDS) to determine the OER efficiency.

For the acidic solution

$$2H_2O \rightarrow OH^* + H^+ + H_2O + e^- \tag{1}$$

$$OH^* + H^+ + e^- + H_2O \rightarrow O^* + 2H^+ + H_2O + 2e^- \tag{2}$$

$$O^* + 2H^+ + 2e^- + H_2O \rightarrow OOH^* + 3H^+ + 3e^- \tag{3}$$

$$OOH^* + 3H^+ + 3e^- \rightarrow O_2 + 4H^+ + 4e^- \tag{4}$$

For the alkaline solution

$$4OH^- \rightarrow OH^* + 3OH^- + e^- \tag{5}$$

$$OH^* + 3OH^- + e^- \rightarrow O^* + 2OH^- + H_2O + 2e^- \tag{6}$$

$$O^* + 2OH^- + H_2O + 2e^- \rightarrow OOH^* + H_2O + OH^- + 3e^- \tag{7}$$

$$OOH^* + H_2O + OH^- + 3e^- \rightarrow O_2 + 2H_2O + 4e^- \tag{8}$$

Therefore, to construct the high-efficiency and reliable OER electrocatalysts, there are many strategies that have been proposed including the optimized structure and morphologies. In general, a large surface area and pore volume are highly needed for an efficient electrocatalyst to expose more active sites for electrocatalysis. Meanwhile, they can also guarantee the fast electron/mass transfer and provide sufficient interfacial regions to promote the reactions. In addition, the easy fabrication and low cost of the electrocatalysts are also significant for future practical applications in green and sustainable energy systems. In addition, the easy fabrication and low cost of the electrocatalysts are also significant for future practical applications in green and sustainable energy systems.[18]

It was found that MOFs with 2D layered structures have a variety of advantages. The nanometer thickness facilitated the mass transfer and rapid electron transfer, resulting in high reaction rates.[19] Moreover, the increased surface area of the accessible surface-active metal sites and the surface coordination of unsaturated metal sites promoted the interaction with the reactive substrates.[20] Therefore, 2D MOF nanomaterials exhibit excellent performance in OER, ORR, and other catalysis reactions. Although 2D MOFs can be directly used as OER electrocatalysts,

there are few reports of MOFs as direct electrocatalysts.[20a,b,21] It is always difficult to reach satisfying levels of robust electrocatalytic water splitting, because of the sluggish kinetics of the OER.[22] To achieve electrocatalysts with high efficiency and low overpotential, the researchers investigated the expected results by combining different organic ligands, metals, heteroatom-doped, substrate, synthesis methods, and other strategies. **Table 1** shows a summary of the various 2D MOFs that have been reported as electrocatalysts for OER along with their activity. In recent years, there have been more researches on the electrocatalysis of 2D MOFs, and the synthesis methods of 2D MOFs are also varied. (These methods can be divided into two categories: top-down and bottom-up methods.)[11c,12b] The activity of an electrocatalyst is usually dependent on factors such as accessibility of active centers, electrical conductivity, and electrode geometry.[23] Each parameter needs to be optimized to improve the catalytic efficiency. The organic ligand is also a key parameter in MOF electrocatalytic materials. The main organic ligands used in the synthesis of MOFs are carboxylate ligands and other negatively charged ligands.[24] Here, we have classified the recently used organic ligands of 2D MOFs for OER into benzene dicarboxylate (BDC), BDC modified with functional groups, naphthalene-based dicarboxylate, dual ligands, N- and S-heterocyclic ligands, and phthalocyanine and porphyrin-based ligands. The 2D MOF materials and their OER characteristics are summarized and described in each section.

2.1. Benzene Dicarboxylate

The most widely applied organic ligands are mainly nitrogen-containing heterocyclic ligands (e.g., 2-methylimidazole and 4,4′-bipyridine) and carboxyl-containing organic ligands (e.g., 2,6-naphthalene dicarboxylate acid and terephthalic acid). In recent years, most 2D MOFs synthesized used compounds containing two or more carboxyl groups as ligands. First of all, the carboxyl group has a larger negative charge density and stronger coordination with metal. Moreover, the carboxyl group and metal ion have various coordination ways, which can form metal carboxylate clusters or bridged linkages. This structure can increase the stability and rigidity of the MOF skeleton. The adjacent carboxyl groups at special angles (e.g., 60°, 120°, 180°) can connect metal ions in special directions, thus obtaining a unique extended network.[25] The 2D MOFs can be directly used as OER electrocatalysts, but there are few reports of MOFs as direct electrocatalysts. The most commonly used ligand in the recently reported 2D MOF materials for OER electrocatalysis was 1,4-benzene dicarboxylic acid (BDC). BDC was a binary aromatic carboxylic acid composed of two carboxylic groups connected to two carbon atoms in the benzene ring. It dissolves in most organic solvents and is cheap. So far, the synthesis methods of 2D MOFs with BDC as the organic ligand mainly include sonication synthesis, solvothermal synthesis, and three-layer synthesis. As BDC has been widely studied as an organic ligand, this part is classified according to the synthesis method of the 2D MOFs.

2.1.1. Sonication Synthesis

The sonication synthesis as an energy-efficient, fast, and environmentally friendly bottom-up synthetic method is the most

Table 1. Comparison of the 2D MOFs for catalyzing OER with reported typical materials in alkaline solution.

Ligand name	Catalyst	Synthesis method	Electrolyte	Overpotential @10 mA cm⁻² [mV]	Tafel slope [mV dec⁻¹]	Substrate	Ref.
1,4-Benzene dicarboxylic acid (BDC)	NiCo-UMOFNs	Sonication synthesis	1 M KOH	250	42	GCE	[20a]
	NiFe-UMNs	Sonication synthesis	1 M KOH	260	30	GCE	[20b]
	Pt-NC/Ni-MOF	Sonication synthesis	1 M KOH	292	42.1	GCE	[31]
	Ni-BDC/Ni(OH)$_2$	Sonication synthesis	1 M KOH	320	41	GCE	[32]
	NiFeZn-MNs/NF	Sonication synthesis	1 M KOH	310	49	NF	[33]
	Ni-MOF@Fe-MOF	Sonication + hybridization	1 M KOH	265	82	GCE	[34]
	Ni-Fe-MOF NSs	Solvothermal	1 M KOH	221	56	GCE	[36]
	2D Ni-MOF-250	Solvothermal	1 M KOH	250@50 mA cm⁻²	88.6	NF	[37]
	2D Co$_3$O$_4$/C$_{BDC}$	Solvothermal	1 M KOH	208	50.1	Ni foil	[40]
	(U + S)-CoFe-MOF	Ultrasound + Solvothermal	1 M KOH	277	31	GCE	[41]
	Ultrathin Co-MOF	Surfactant assisted	1 M KOH	263	74	GCE	[42]
	Ti$_3$C$_2$T$_x$ – CoBDC	Three-layer synthesis	0.1 M KOH	410	48.2	GCE	[44]
2,5-dihydroxyterephthalic acid (H$_2$dobdc)	Fe$_2$O$_3$@Ni-MOF-74	Solvothermal	1 M KOH	264	48	GCE	[123]
2,3-dihydroxy-1,4-benzenedicarboxylic acid (H$_4$dhbdc)	FeCo-MNS-1.0	Hydrothermal	0.1 M KOH	298	21.6	NF	[48]
	Fe:2D-Co-NS	Solvothermal	0.1 M KOH	211	43	NF	[52]
2-aminoterephthalic acid (NH$_2$-BDC)	Co$_3$Fe-MOF	Sonication synthesis	1 M KOH	280	38	GCE	[54]
Tetrafluoroterephthalic acid (H$_2$TFBDC)	CoTFBDC/EG-250	Three-layer synthesis	1 M KOH	380	39.8	RDE	[57]
2,6-naphthalene dicarboxylate acid (NDC)	CoNi(1:1)-MOF	Hydrothermal	1 M KOH	265	56	Cu Foil	[60]
2,6-naphthalene dicarboxylic acid dipotassium (K$_2$NDC)	NiFe-MOF	Chemical bath deposition	0.1 M KOH	240	34	NF	[23]
	CoNi-NDC/PANI-NF	Hydrothermal	1 M KOH	323	73.3	NF	[124]
Terephthalic acid(A); 2-aminoterephthalic acid(B)	A$_{2.7}$B-MOF-FeCo$_{1.6}$	Solvothermal	1 M KOH	288	39	GCE	[63]

Table 1. Continued.

Ligand structure	Ligand name	Catalyst	Synthesis method	Electrolyte	Overpotential @10 mA cm^{-2} [mV]	Tafel slope [mV dec^{-1}]	Substrate	Ref.
	Terephthalic acid; 4,4′-(sulfonylbis(4,1-phenylene))dipyridine(SPDP)	Co$_9$S$_8$@TDC	Solvothermal	1 M KOH	330	62	GCE	[64]
	Terephthalic acid (BDC); Ferrocenecarboxylic acid	CoBDC-Fc-NF	Solvothermal	1 M KOH	178	51	NF	[125]
	Terephthalic acid (BDC); 1,4-Diazabicyclo[2.2.2]octane (DABCO)	HXP@NC800	Bottom-up synthesis	1 M KOH	307	48	GCE	[67]
	Terephthalic acid (BDC); 4,4′-biphenyldicarboxylate (BPDC)	Co-BPDC/Co-BDC	Two step	1 M KOH	335	72.1	GCE	[68]
	4,4′-bipyridine	Py-1@SNC600	Solvothermal	1 M KOH	284.7	56	NF	[66]
	2-methylimidazole(2MeIm)	Fe$_1$Co$_3$/VO-800	RF plasma treatment	1 M KOH	260	53	CC	[72]
		D-U-Co(OH)$_2$	Room-temperature solution phase method	1 M KOH	223	131	NF	[73]
	4,5-Imidazoledicarboxylic acid	CoFe-MOF-OH	Hydrothermal	1 M KOH	265	48	GCE	[74]
	Hypoxanthine (HPA)	Co-Ni@HPA-MOF	Hydrothermal	1 M KOH	320	58	GCE	[78]
	2,5-furandicarboxylate (FDC)	2D Cu$_2$O/C$_{FDC}$	Solvothermal	1 M KOH	352	84.7	Cu foil	[40]
	Thiophenedicarboxylate acid(H$_2$TDC)	Co-MOF/NF	Hydrothermal	1 M KOH	270	75	NF	[79]
		2D Cu$_2$O/S-C$_{TDC}$	Solvothermal	1 M KOH	313	65.6	Cu foil	[40]
	2,3,9,10,16,17,23,24-octa-aminophthalocyaninato nickel(II) (NiPc-NH$_2$)	NiPc-MOF	Bottom-up approach	1 M KOH	350	74	FTO	[84]
	4,4′,4″,4‴-((4,4′,4″,4‴-(porphyrin-5,10,15,20-tetrayl)tetrakis(benzoyl))tetrakis(azanediyl)) tetrabenzoic acid (TCPP)	Co-P@/NC-800	Solvothermal	1 M KOH	370	79	GCE	[89]
	Copper (II) meso-tetra(4-carboxyphenyl) porphyrin (CuTCPP)	Co-CuTCPP/rGO-10	Hydrothermal	1 M KOH	396	58	GCE	[90]

**ADVANCED
SCIENCE NEWS**
www.advancedsciencenews.com

**ADVANCED
ENERGY & SUSTAINABILITY
RESEARCH**
Open Access
www.advenergysustres.com

common way to prepare 2D MOFs.[11c,12b] More importantly, the method can be applied to the direct synthesis of 2D ultrathin MOF nanosheets (UMNs).[20a,b] Taking the synthesis of NiCo–bimetal ultrathin metal–organic framework nanosheets (NiCo-UMOFNs) as an example, metal ions and organic ligands (BDC) were first dissolved in the mixture solvent system that consisted of N,N-dimethylformamide (DMF), H_2O, and ethanol and then trimethylamine is also added. After stirring to form a colloidal suspension, NiCo-UMOFNs were prepared by continuous ultrasound for 8 h (40 kHz) under air-tight conditions.[20a] It has been identified that the metal sites are linked in the (200) plane, which forms 2D bimetal layers. With separation by the BDC ligands, the crystal structure of MOFs is formed. The overpotential for NiCo-UMOFNs on glassy carbon electrodes (GCE) was only 250 mV at the current density of 10 mA cm^{-2}. NiCo-UMOFNs exhibit the small Tafel slope of 42 mV dec^{-1}. Density functional theory (DFT) calculations indicated that the unsaturated environment of the local metal atoms play as the active centers, in which the strong coupling effect between Ni and Co metals becomes the key factor to modulate the electrocatalytic activity.

Following the same strategy, 2D bimetals (CoFe and NiFe) UMNs were achieved through the introduction of BDC as the ligand.[20b] All the structure characterization methods confirmed the 2D ultrathin morphology of the obtained NiFe-UMNs (**Figure** 1a,b). Due to the coordinative contribution of more unsaturated active metal sites on the surface, the catalytic activity improves. This is attributed to the nanometer thickness and the unique bonding environment induced by BDC ligands.[19,20c,26] In comparison, the bulk 3D NiFe-MOFs was synthesized by a hydrothermal method. The performance of NiFe-UMNs exhibits superior performance to the bulk NiFe-MOFs and CoFe-UMNs with a 260 mV overpotential to reach the current density of 10 mA cm^{-2} and a small Tafel slope of 30 mV dec^{-1}. The performance difference is determined by the structural advantage of the 2D layered structure and the intrinsical electroactivity of Ni.[27] DFT calculations were carried out to investigate the reaction mechanism,[28] which has carefully considered the OER process (Figure 1c,d), including the initial adsorption of reactants, the intermediates transformation, and final desorption of formed O_2. For the key intermediates OH*, NiFe-UMNs showed a much lower energy cost for stable adsorption, supporting an energetically preferred process (Figure 1d). The Gibbs free energy of the initial adsorption was inversely proportional to the adsorption strength of OH$^-$. For the OER process, the conversion between O* to *OOH in step iii is usually considered as the RDS to determine electroactivity. Among different active sites, it is noted that Ni sites in NiFe-UMNs show the lowest value of ΔG_3, of 1.20 eV, supporting the highest electroactivity. The Fe sites in NiFe-UMNs show a slightly higher ΔG_3. However, the NiFe-UMNs support a higher electroactivity than CoFe-UMNs due to the lower energy barrier of the RDS. X-ray photoelectron spectroscopy (XPS) showed that the addition of Fe could generate a higher valence state in Ni, which possessed a stronger ability to accept electrons and accelerated the charge transfer.[20b,29] Therefore, the combination of Fe and Ni could significantly reduce the energy barrier and provide better OER activity.

With the appropriate modulation of the intermediates in electrocatalysis, the electrocatalytic performance will be significantly optimized. Both hydrogen evolution reaction (HER) and OER involve intermediates of OH* and H*.[30] Recently, Qiao and coworkers[31] successfully modulated the intermediates of OER through the interfacial bonding approach on the Pt-NC/Ni-MOF structure. The optimized Pt-NC/Ni-MOF demonstrates three layers of sandwiched slab structures, which consist of Pt atoms and newly formed Ni—O—Pt bonds and Ni-MOFs (Figure 1e). Charge difference analysis indicated electron relocation due to the formation of a heterostructure, which confirmed a charge transfer between the Ni-MOFs and the Pt-NC side at the heterostructure interface. The charge accumulation is mainly located near the Ni—O—Pt bond. Both OH* adsorption (on the Ni-MOF surface) and H* adsorption (on the Pt surface) are correspondingly modified at the heterostructure due to the inhomogeneous electronic distribution (Figure 1f,g). On the Ni-MOF side, OH* adsorption becomes stronger, with an adsorption energy of −0.61 eV. Meanwhile, the theoretical calculation revealed the charge distribution on the Ni—O—Pt bond. This modulated electronic structure shows the stronger H* adsorption strength whereas the adsorption of OH* becomes weaker (Figure 1h,i). The simultaneous optimization of intermediates binding is attributed to the electron density increase and the modulated Ni 3d orbitals.

Through the similar ultrasonic method, Zhu et al.[32] further synthesized novel 2D Ni–BDC/Ni(OH)$_2$ hybrid nanosheets (NSs) from the mixture of Ni^{2+}, Ni(OH)$_2$ NSs, and BDC, which demonstrates the high surface area from Ni-BDC. Importantly, the electronic structure of Ni sites in the Ni(OH)$_2$ component has been modified after coupling, which induces the high valence states of Ni. Such electronic structures are desirable for the OER, supporting the excellent OER performances of this hybrid NS. The overpotential for Ni-BDC/Ni(OH)$_2$, 320 Mv, at the current density of 10 mA cm^{-2}, surpasses all the comparison samples, with Ni-BDC of 358 mV, Ni(OH)$_2$ NSs of 395 mV, and Ir/C of 332 mV. Moreover, Ni-BDC/Ni(OH)$_2$ showed the lowest Tafel slope of 41 mV dec^{-1}. Wei et al.[33] reported another type of 2D ultrathin MOF, NiFeZn–MNs/Ni foam (NF) NSs, containing a few metal oxide nanoparticles (NPs). This material has been fabricated by the sonication-assisted solution method and grown on the Ni foam, which can augment the electrode–electrolyte interface and minimize ohmic loss. Compared with other MOF-based electrocatalysts, the NiFeZn–MNs/NF catalyst shows remarkable electrocatalytic performance. Even at the high current density of 50 mA cm^{-2}, the overpotential of NiFeZn–MNs/NF is only 350 mV. After 120 h of the stability test, such a superior electrocatalytic performance is still well preserved with only 5% drop at the current density.

The catalytic activity can be significantly improved by anchoring Fe-MOF NPs with poor electroactivity on the electroactive UMNs. 2D Ni-MOF@Fe-MOF NS hybrid materials were fabricated by stepwise synthesis at room temperature (**Figure 2**a).[34] Based on the liquid exfoliation approach, the 2D Ni-MOF NSs were prepared with the ultrasonic approach. The thickness of the Ni-MOF NSs was confirmed by the atomic force microscopy (AFM), which is equal to about ≈5–6 layers of the coordination structures. In the mixed DMF/H_2O/ethanol solvent system, the prepared Ni-MOF NSs were anchored with Fe-MOF NPs through an in situ surface-anchoring of Fe (III) and BDC ligand (Figure 2b). Without the Ni-MOF NSs, Fe-MOF NPs
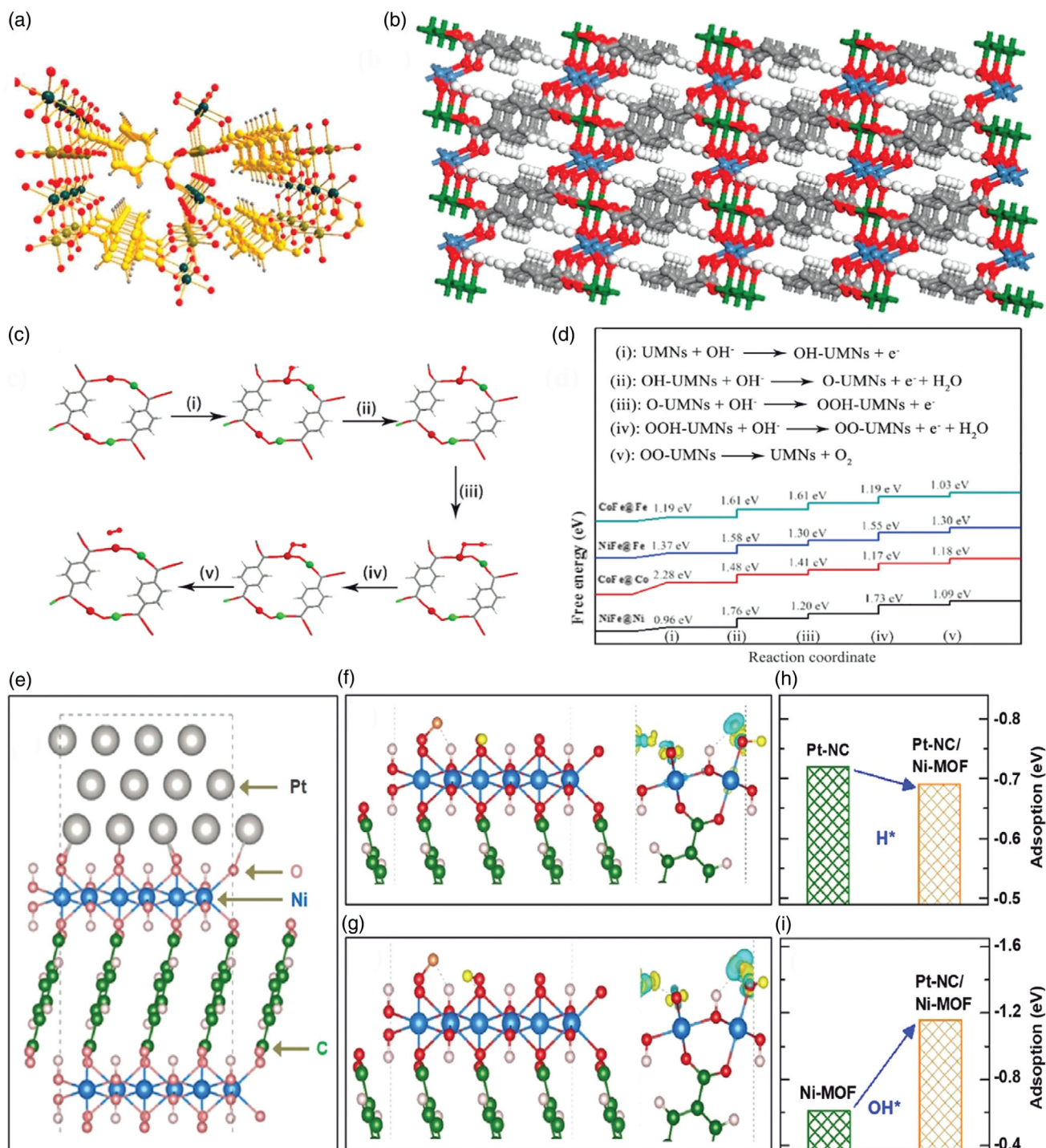
Figure 1. a) The crystal structure of NiFe-UMNs; b) atomic arrangements of NiFe-UMNs; c) reaction steps of the OER processes; d) Gibbs free energy diagrams for CoFe-UMNs and NiFe-UMNs during the OER processes. (a–d) Reproduced with permission.[20b] Copyright 2018, Elsevier. e) Atomic model of Pt-NC/Ni-MOF heterostructure. f,g) Dissociative OH* adsorption and charge difference analysis on the stand-alone Ni-MOF structure (f) and on the Ni-MOF side of the Pt-NC/Ni-MOF structure (g); h) H* adsorption energy; i) OH* adsorption energy. (e–i) Reproduced with permission.[31] Copyright 2019, Elsevier.

display evident agglomeration X-ray diffraction (XRD) that revealed that Ni-MOF@Fe-MOF and pristine Ni-MOF exhibit identical crystal phases, where the peaks are assigned to (200),

(-201), and (400) planes of a monoclinic structure. The Ni/Fe atomic ratio measured by inductively coupled plasma optical emission spectrometer (ICP-OES) analysis was 3.5/1. XPS
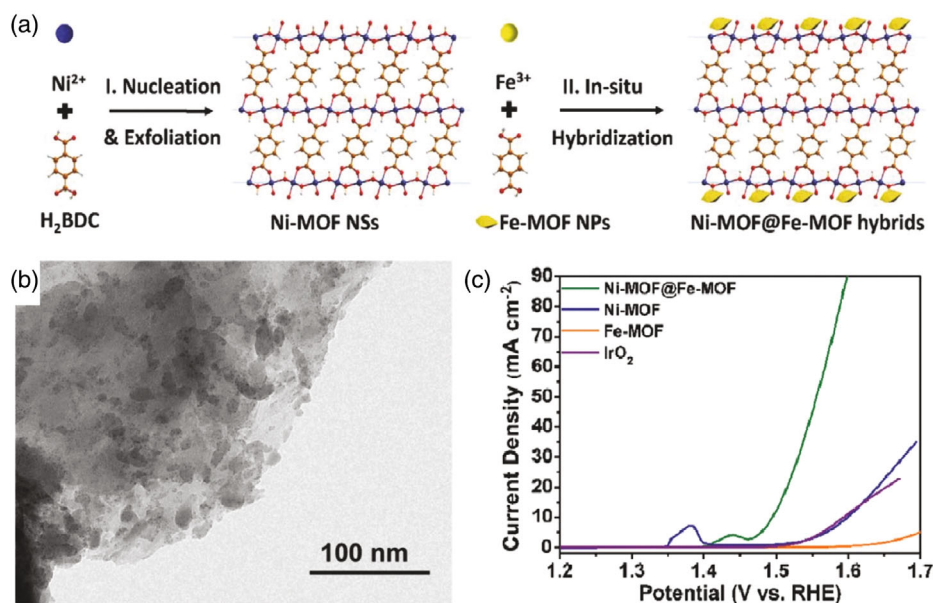
**ADVANCED
SCIENCE NEWS**

www.advancedsciencenews.com

**ADVANCED
ENERGY & SUSTAINABILITY
RESEARCH**
Open Access

www.advenergysustres.com

Figure 2. a) Synthesis of Ni-MOF@Fe-MOF hybrid NSs; b) transmission electron microscope (TEM) images of the Ni-MOF@Fe-MOF hybrid; c) linear sweep voltammetry (LSV) curves toward OER in O_2-saturated 1.0 M KOH with a scan rate of 5 mV s^{-1}. (a–c) Reproduced with permission.[34] Copyright 2018, Wiley-VCH Verlag GmbH & Co. KGaA.

confirmed the existence of Ni^{2+} in the Ni-MOF@Fe-MOF hybrid NSs. The Ni-MOF@Fe-MOF hybrid NSs show high OER electroactivity, and the NSs were not treated by annealing. The lowest overpotential of Ni-MOF@Fe-MOF was 265 mV at a current density of 10 mA cm^{-2} that is lower than that of the state-of-the-art OER catalyst IrO_2 (365 mV). The pristine Ni-MOF shows poor electroactivity to the water oxidation reaction. However, the hybridization with Fe-MOF enables the significant decrease in overpotential for Ni-MOF (370 mV) by ≈100 mV (Figure 2c). Furthermore, the reaction mechanism has been studied through the rotating ring-disk electrode (RRDE) technique, with the fixed-ring electrode potential achieving the oxidization of the surface peroxide intermediates. Compared with the disk, the ring current density is three orders of magnitude lower, indicating the absence of hydrogen peroxide, which guarantees an efficient four-electron pathway for water oxidation.

2.1.2. Solvothermal Synthesis

The solvothermal method is a common and effective method for the synthesis of 2D MOFs. The solvothermal process was completed by chemical transmission.[35] Usually, the metal salt and organic ligand were dissolved in the solvent, and the mixed solution reacted in the reaction vessel at a certain temperature and autogenic pressure to obtain the target product. The organic solvent plays a key role in controlling the formation of 2D MOFs. Commonly used solvents include ethanol, methanol, DMF, etc. MOFs with excellent performance can be synthesized by controlling the ratio of reactants, pH value of the system, temperature, and other factors. The main features of this method are easy operation, low cost and the ability to synthesize nanomaterials with special morphology and excellent performance. The

solvothermal method is more efficient in terms of yield compared with the sonication synthesis method.[36]

The scale synthesis of 2D UMNs with uniform morphologies and the integrated structures is still challenging. Recently, Li et al. reported that the bottom-up solvothermal method could be used for large-scale preparation of 2D UMNs with a thickness of only several atomic layers (**Figure 3**a).[36] Based on the appropriate mixture of N,N-dimethylacetamide and water solvents, the Ni–Fe-MOF NSs are successfully synthesized. With water as the only solvent, we notice the formation of the amorphous nanoflowers with the NPs. In comparison, the porous flowers are formed when the solvent becomes N,N-dimethylacetamide. Only the organic solvent with good solubility for organic ligands is able to facilitate the synthesis of Ni–Fe-MOF NSs. The AFM image determined that the thickness of the NSs ranged from 1.67 to 2.58 nm with an interlayer distance of 0.928 nm. The Ni–Fe-MOF NSs exhibited excellent OER performance with an overpotential of 221 mV at the current density of 10 mA cm^{-2}, much smaller than that of the monometallic Ni-MOF NSs (386 mV) and Ir/C (311 mV). It also showed a smaller Tafel slope of 56.0 mV dec^{-1} than that of monometallic Ni-MOF NSs (106.1 mV dec^{-1}) and Ir/C (59.2 mV dec^{-1}). DFT calculations of the energy barriers for OER at different metal sites confirmed that Fe was the active site for OER in the Ni–Fe-MOF NSs. According to the DFT calculations, possible mechanisms for OER in different metal locations were proposed (Figure 3b). For the Fe@Ni1-MOF (020) surface, two protons are detached from the two μ-OH ligands to connect the Ni and Fe sites. Then two coordinated H_2O molecules also are deprotonated and form two adsorbed OH ligands, producing electroactive HOOH species to facilitate the formation of O_2. Thus, the Fe site in Fe@Ni1-MOF shows a remarkable electrochemical performance (Figure 3c,d).
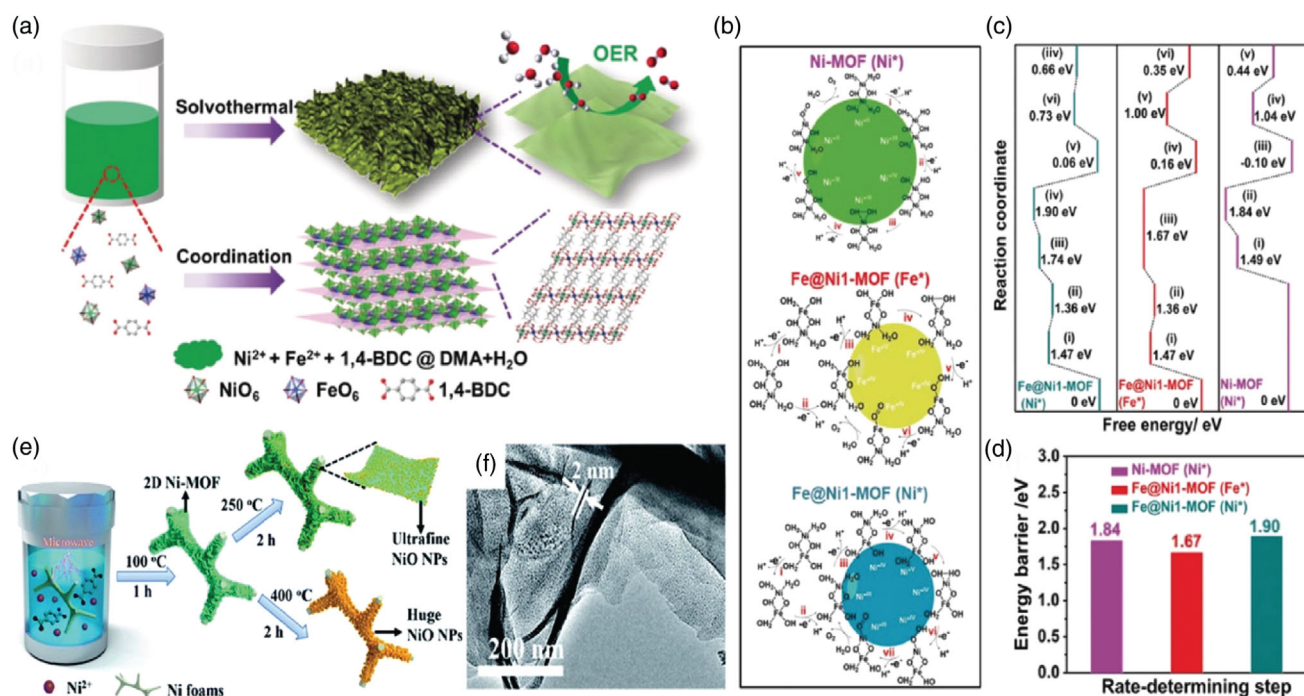
Figure 3. a) Synthesis of 2D UMNs and their utilization for the OER; b) the most probable OER reaction mechanisms; c) The kinetic energy barrier distribution of products and intermediates on Fe@Ni1-MOF(Ni*), Fe@Ni1-MOF(Fe*), and Ni-MOF(Ni*); d) energy barrier comparison for the RDS on Fe@Ni1-MOF(Ni*), Fe@Ni1-MOF(Fe*), and Ni-MOF(Ni*). (a–d) Reproduced with permission.[36] Copyright 2019, Wiley-VCH Verlag GmbH & Co. KGaA. e) In situ growth of 2D Ni-MOF NSs on the substrate by a microwave-assisted solvothermal method; f) TEM image of 2D Ni-MOF-250. (e,f) Reproduced with permission.[37] Copyright 2020, Royal Society of Chemistry.

The ultrathin 2D Ni-MOF NSs can be fabricated quickly and easily (e.g., 1 h) by the microwave-assisted solvothermal method under surfactant-free conditions. The thickness of the NSs is around 2 nm, which were grown in situ on Ni foams at 100 °C (Figure 3e).[37] The microwave can modulate growth kinetics during nucleation, which is the key factor to facilitate the formation of specific nanostructures (e.g., NSs).[38] Based on the strong resonance, microwave radiation promotes the interaction with reactants and speeds up the solvothermal procedure for the growth.[39] Subsequently, the ultrafine nickel oxide (NiO) NP was formed on the Ni-MOF NSs. The controllable calcination at 250 °C will not influence the 2D morphology of Ni-MOF whereas the ultrafine NiO NPs have been formed (Figure 3f). However, the direct high-temperature calcination at 400 °C will cause the sharp collapse of the ultrathin 2D structure rather than the NSs, which results in the formation of huge NiO aggregates. The overpotential of 2D Ni-MOF-250 was 250 mV at a current density of 50 mA cm^{-2}, which is much smaller than those samples calcined at 250 and 400 °C. More importantly, such a material also demonstrates over 20 h stability at the current density of 110 mA cm^{-2}. The charge transfer resistance results supported the much smaller resistance of 2D Ni-MOF-250 than other comparison samples. In addition, the double-layer capacitance (C_{dl}) value of 2D Ni-MOF-250 was 11.5 mF cm^{-2}, which was larger than those of 2D Ni-MOF (7.8 mF cm^{-2}) and 2D Ni-MOF-400 (6.9 mF cm^{-2}). These results indicated that the controllable calculations at 250 °C preserved the 2D structure, which provided additional active sites for OER.

Transition metal oxides have become the most widely studied OER electrocatalysts. However, the slow mass transfer, low electrical conductivity, and inadequate active sites still limit their electroactivity. Zhou et al. constructed metal oxide/carbon (MO_x/C, M = Co, Ni, and Cu) NS arrays using 2D MOFs as templates by the solvothermal method.[40] The layered 2D MOF structures usually possess abundant hierarchical pores, which guarantee more exposed active sites and improved conductivity. 1,3,5-benzenetricarboxylic acid (BTC), BDC, and 2,5-dihydroxyterephthalic acid (DHTP) combine with Co^{2+} to form Co-BTC, Co-BDC, and Co-DHTP arrays, respectively. The 1D Co_3O_4/C_{BTC}, 2D Co_3O_4/C_{BDC}, and 3D Co_3O_4/C_{DHTP} arrays were prepared by the pyrolysis treatment of Co-BTC, Co-BDC, and Co-DHTP arrays at 600 °C for 2 h under high-purity N_2 gas flow, respectively. The OER performance of 2D Co_3O_4/C_{BDC} was better than that of 1D Co_3O_4/C_{BTC} and 3D Co_3O_4/C_{DHTP} with the overpotential of 208 mV at the current density of 10 mA cm^{-2} and Tafel slope of 50.1 mV dec^{-1}.

The (U + S)-CoFe-MOF (U = ultrasound synthesized, S = solvothermal prepared) was synthesized by a two-step synthesis method.[41] First, 2D MOFs were synthesized by ultrasonic-assisted synthesis, and then the unstable MOF domain was removed by solvothermal treatment, which creates continuous mesopores on the 2D MOFs with abundant boundaries. Significantly, more active sites were generated due to the metal ions transforming from M—OOH into M—O/M—OH (M = Co or Fe) after the second solvothermal step. Through ultrasonic synthesis, the 2D CoFe-MOF is synthesized with a thickness

of 1.3 nm. With solvothermal etching, hierarchical porosity on the MOF is achieved without loss of the NSs morphology. In contrast, the MOFs prepared by only ultrasound show limited porosity and the MOFs prepared from the direct solvothermal method display a much larger thickness. The hierarchical 2D CoFe-MOFs yield an overpotential of 277 mV at the current density of 10 mA cm^{-2} and Tafel slope of 31 mV dec^{-1}, which are better than the MOFs prepared by only ultrasonic (300 mV, 40 mV dec^{-1}) and solvothermal methods (310 mV, 57 mV dec^{-1}). Pang and coworkers[42] have used the simple surfactant-assisted hydrothermal method to realize the ultrathin Co-MOF NSs with BDC as the organic ligand. Such a material shows good catalytic activity for the OER. Polyvinylpyrrolidone (PVP), as the anionic surfactant, significantly improves the growth of MOFs in the vertical direction. AFM showed that the ultrathin Co-MOFs had a thickness of 1.941 nm. On the ultrathin Co-MOF NS surface, part of the Co centers shows the coordination number 5 due to the limitation of edge growth. At these sites, the bindings of solvent/reactant molecules are reversible. For comparison, bulk Co-MOFs and micro–nano Co-MOFs were prepared. The double-layer capacitance (C_{dl}) value of ultrathin 2D Co-MOF NSs was 20.36 mF cm^{-2}, which was superior to the larger-size comparison samples of micro–nano Co-MOFs and bulk Co-MOFs. The larger C_{dl} value usually indicates the greater roughness of the corresponding electrode as well as more active sites. The overpotential for ultrathin Co-MOFs on GCEs was ≈263 mV at the current density of 10 mA cm^{-2}. Ultrathin Co-MOFs exhibit the small Tafel slope of 74 mV dec^{-1} with electrochemical stability for over 5 h. The excellent OER performance was mainly attributed to the porous structure of ultrathin 2D

NSs, the cooperation of unsaturated active sites, and rapid ion transport.

2.1.3. Three-Layer Synthesis

Three-layer synthesis is also a widely used bottom-up method. The layering technique can control the crystal growth by slowing the diffusion and growth rate.[43] This method uses two different densities of miscible solvents. The lower-density solvent on top and a higher-density solvent at the bottom, in which a buffer zone is located in the middle, lead to the construction of the three-layer structure. For instance, the three-layer synthesis method has been reported to fabricate 2D Ti$_3$C$_2$T$_x$–CoBDC NSs using a mixture of acetonitrile (CH$_3$CN)/DMF solvents with different ratios.[44] Higher-density DMF is located at the bottom, whereas the lower-density CH$_3$CN shows a higher concentration in the top layer, and the middle layer contains a mixture of CH$_3$CN and DMF as the buffer. With different densities of solvents, metal ions and the organic ligands (BDC) are dissolved in the top and bottom layers, respectively. The middle buffer layer aims to slow down the diffusion and growth rate. The diffusions of metal ions and organic ligands to the middle layer results in the dilution of the precursors, which prefers the formation of thin 2D MOF NSs under the static condition.

The three-layer synthesis method is an important method for the synthesis of 2D MOF NSs. The MXene/MOF hybrid (Ti$_3$C$_2$T$_x$–CoBDC) was successfully synthesized by this surfactant-free method (**Figure 4**a).[44] The metal-like Ti$_3$C$_2$T$_x$ (the MXene phase, T$_x$ represents surface groups) NSs were used as the template to realize the in situ deposition of the 2D

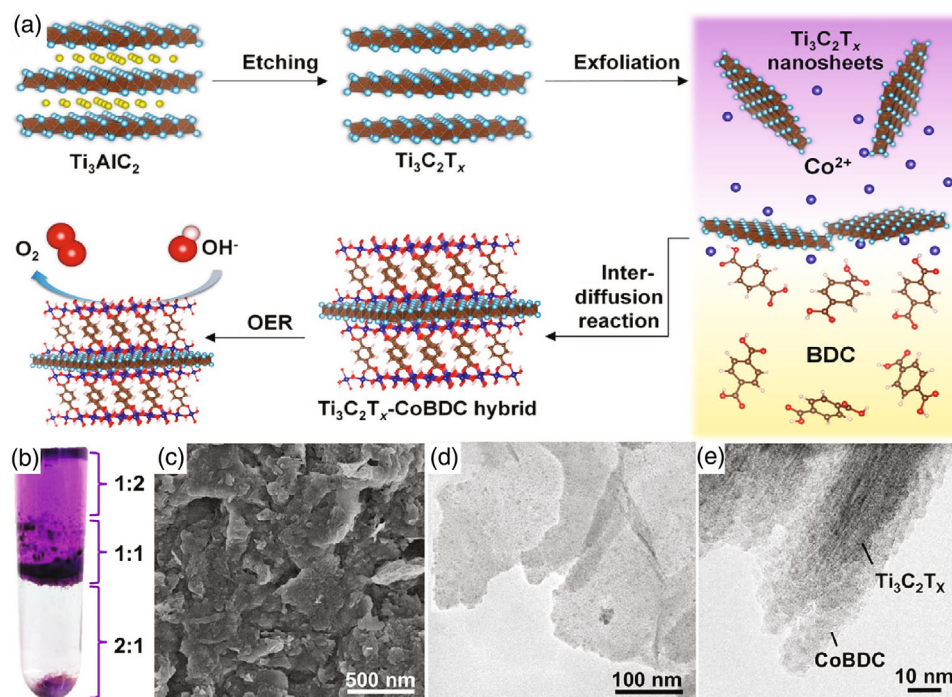**Figure 4.** a) The preparation process of Ti$_3$C$_2$T$_x$–CoBDC hybrid for OER; b) photograph of a test tube taken during the preparation of Ti$_3$C$_2$T$_x$–CoBDC via an interdiffusion reaction; c) scanning electron microscope (SEM) image; d) TEM image of the Ti$_3$C$_2$T$_x$–CoBDC hybrid NSs; e) cross-sectional view of a stacked Ti$_3$C$_2$T$_x$–CoBDC hybrid. (a–e) Reproduced with permission.[44] Copyright 2019, American Chemical Society.

CoBDC via an interdiffusion reaction. The reaction was conducted in a test tube with the mixture DMF and acetonitrile (CH_3CN) solvent, where we noticed the formation of a three-layered solution. The DMF/CH_3CN volume ratios vary in different layers, which demonstrate the ratios of 2:1, 1:1, and 1:2 from the top to the bottom layer (Figure 4b). The Co^{2+} ions with the $Ti_3C_2T_x$ NSs and BDC were dissolved into the top and bottom layers of the solution, respectively. In the top layer, the functional groups such as the $Ti_3C_2T_x$ NS surface are able to adsorb Co^{2+} ions due to the electrostatic interaction. Under gravity, the NSs in the top layer migrate to the middle layer of the solution. The Co^{2+} adsorbed on the surface facilitates the diffusion of the formed coordinated molecules from the bottom to the middle layer, which promotes the formation of $Ti_3C_2T_x$–CoBDC mixture. Such a mixture gradually sinks due to gravity force. The $Ti_3C_2T_x$–CoBDC hybrid material showed a similar morphology to the NS (Figure 4c,d), but the CoBDC surface was rough due to surface deposition. CoBDC was tightly covered on the surface of the $Ti_3C_2T_x$ NS (Figure 4e). XPS confirmed that the hybridization with $Ti_3C_2T_x$ did not induce the change of the oxidation states of Co species in CoBDC. Notably, the conductive $Ti_3C_2T_x$ NSs play a key role by altering the OER to a reaction-limited process with significantly enhanced charge transfer kinetics. The performances of CoBDC, $Ti_3C_2T_x$, and IrO_2 were also compared under the same conditions. The lowest onset potential of the $Ti_3C_2T_x$–CoBDC-modified electrode was 1.51 V versus reversible hydrogen electrode (RHE). For OER, the hybrid catalyst $Ti_3C_2T_x$–CoBDC demonstrated a current density of 10 mA cm^{-2} at a potential of 1.64 V versus RHE, which surpassed the state-of-the-art OER catalyst IrO_2. It is also one of the best-reported OER catalysts under the same catalyst loading measurement conditions.

2.2. BDC Modified with Functional Groups

Many different functional groups (e.g., –Br, –F, –OCH$_3$, –OH, and –NH$_2$) have been introduced into the BDC to create intrinsic strain and defects and optimize the binding energies of intermediates to achieve an enhanced OER activity.[45] The generated strain that optimizes the interaction of reaction intermediates and the surface of the catalyst further increases the OER activity.[46] For instance, Li et al.[46a] experimentally introduced functional groups such as –NH$_2$, –OCH$_3$, and –Br into organic ligands (BDC). The calculation of the electron affinities (the ability of the molecules to get electrons) of BDC-X (X = NH$_2$, H, OCH$_3$, and Br) was carried out to better understand the optimization of the OER activity by changing the functional groups of BDC. Low electron affinities of the ligands can increase the density of the unoccupied states of the transition metals and further enhance their OER activity.[47] The calculations showed that BDC-NH$_2$ had the lowest electron affinity (0.18 eV), whereas BDC-Br had the highest electron affinity (0.66 eV). The results match well with the measured trend, in which NiFe-BDC(NH$_2$) showed the highest OER activity (the overpotential was only 210 mV at the current density of 200 mA cm^{-2}) whereas NiFe-BDC(Br) showed the lowest OER activity in the whole potential range above 1.45 V versus RHE. These functional groups were divided into electron-donating groups and electron-absorbing groups. The main method of synthesis used for these ligands was the hydrothermal/solvothermal method.

2,5-dihydroxyterephthalic acid (H$_4$dobdc) has been selected as the organic ligand to assist the 2D oxide sacrifice approach (2D OSA) to synthesize the 2D ultrathin MOF-74 NSs (M-MNS).[48] The amorphous metal oxide NSs (M-ONS) are synthesized through the sodium borohydride reduction method[49] under ultrasonication, which were slowly added into the DMF/ethanol/water mixed solution containing a suitable amount of H$_4$dobdc. The 2D MOF NSs were obtained by hydrothermal reaction with acidic H$_4$dobdc solution at 100 °C for 24 h (**Figure 5**a). It is identified that the increase in the metal ions next to the metal oxide surface will promote the confined growth of 2D MOFs, which is usually achieved by the leaching of metal ions in M-ONS by the acidic ligand solution (Figure 5b,c). In addition, the dosage of the organic ligand significantly affects both the final morphology and actual crystal structure of MOFs. FeCo-MNS-2.0, FeCo-MNS-1.0, and FeCo-MNS-0.4 are fabricated based on the molar ratios of H$_4$dobdc/FeCo-ONS at 2.0, 1.0, and 0.4, respectively. The AFM showed that FeCo-MNS-1.0 had a thickness of ≈2.6 nm (Figure 5d). The shortage and excess of ligand molecules were not conducive to the conversion of FeCo-ONS into 2D MOF-74 NSs. The XRD patterns confirmed that the MOF crystal grows preferentially along the (300) direction in the beginning of the reaction. The selectivity of the directional growth towards (110) plane becomes stronger in the later reaction (Figure 5e). The overpotential for FeCo-MNS-1.0 was only 298 mV at the current density of 10 mA cm^{-2}, which is considerably smaller than those for FeCo-MNS (318 mV), FeCo-MNS-0.4 (309 mV), and FeCo-MNS-2.0 (312 mV). The mechanism studies revealed that the excellent OER activity of FeCo-MNS-1.0 are due to the heteroatom synergy between Fe and Co and the abundant coordinatively unsaturated metal sites (Figure 5f). The extended X-ray absorption fine structure (EXAFS) data verified that the coordination numbers for Fe ligand and Co ligand of FeCo bulk MOF-74 (FeCo-MB) were both 5.0, supporting the theoretical coordination numbers of MOF-74.[50] However, the coordination numbers for the Fe ligand and Co ligand for FeCo-MNS-1.0 were evidently reduced to 4.0 and 4.5, respectively, which indicates the generation of unsaturated metal sites.

The major obstacles to the synthesis of 2D materials or ultrathin NSs from MOFs are their relatively strong interlayer interactions (e.g., π–π, hydrogen bonds) and relatively weak interlayer bonding (e.g., coordination bonds).[1,51] Recently, 2D MOF materials were synthesized by electrochemical/chemical exfoliation, in which the catechol-functionalized ligand was applied as the redox-active support to construct a pillared-layer framework (**Figure 6**a).[52] The solvothermal reaction of Co^{2+} and 2,3-dihydroxy-1,4-benzenedicarboxylic acid (H$_4$dhbdc) in the ethanol/water mixed solvent leads to the rectangle-shaped crystals of a metal–carboxylate framework 3D Co. The 3D-pillared-layered MOFs served as electrocatalysts for water oxidation, where the pillar ligands were removed after oxidation, leaving the well-maintained ultrathin NSs of the metal–organic layers. Through controlled experiments under various conditions, it was found that 3D Co can evolve into the 2D-Co-NS in the saturated electrolyte with O_2. The crystalline phase was captured based on the periodically stacking 2D NSs (2D-Co), which can
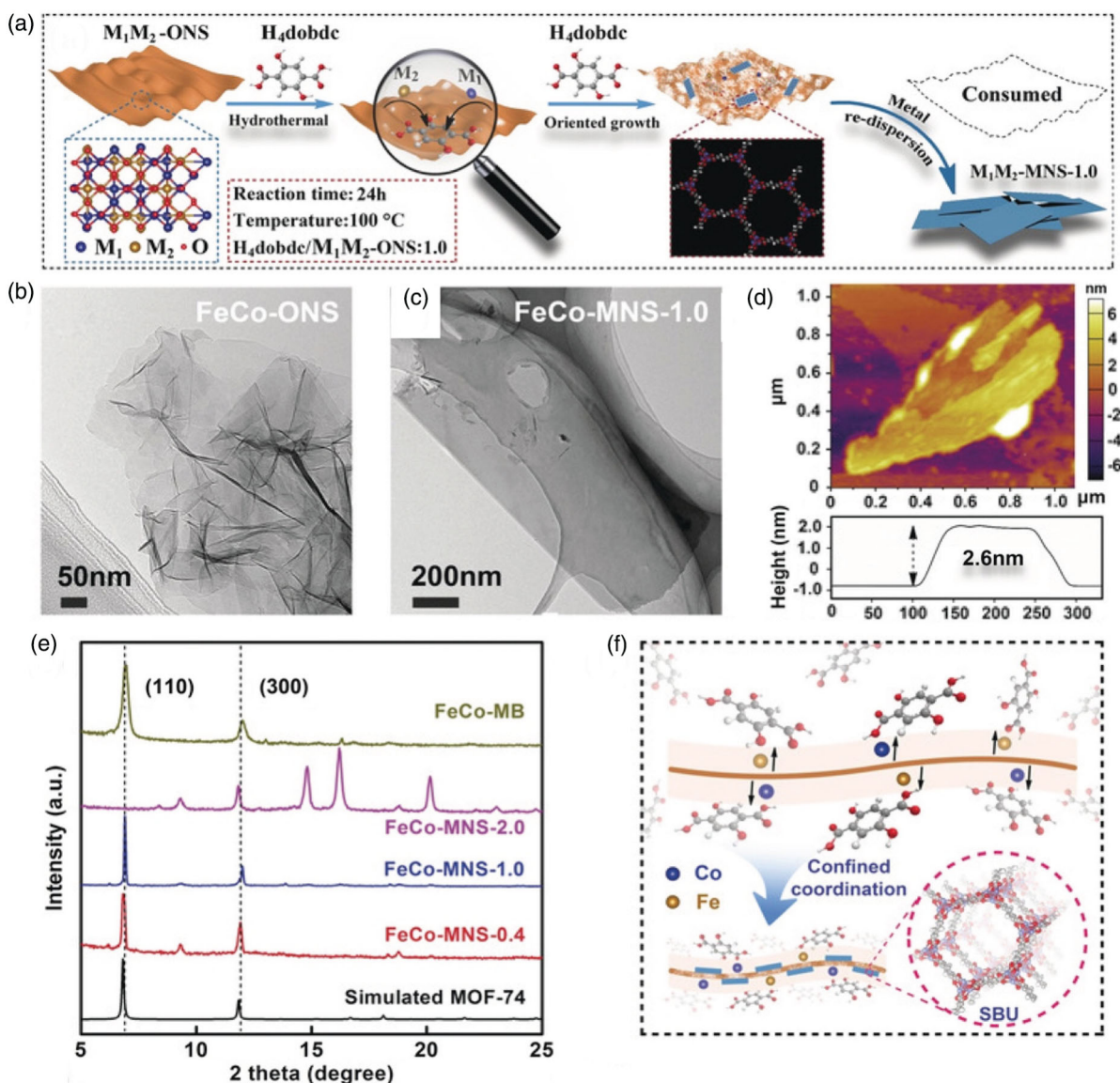
**ADVANCED
SCIENCE NEWS**

www.advancedsciencenews.com

**ADVANCED
ENERGY & SUSTAINABILITY
RESEARCH**
Open Access

www.advenergysustres.com

Figure 5. a) Schematic of the 2dOSA conversion of M-ONS with H$_4$dobdc to form M-MNS; b) SEM image of FeCo-ONS; c) TEM image of FeCo-MNS-1.0; d) AFM image of FeCo-MNS-1.0; e) XRD patterns of FeCo-MB, FeCo-MNS-2.0, FeCo-MNS-1.0, and FeCo-MNS-0.4; f) illustration of the confined growth mechanism of FeCo-MNS adjacent to the FeCo-ONS. (a–f) Reproduced with permission.[48] Copyright 2019, Wiley-VCH Verlag GmbH & Co. KGaA.

further transform to 2D-Co-NS as the intermediate phase identified by the in situ characterizations. The electrochemical exfoliation mechanism of the electrolyte solution and the acid-dissociation catalyst was studied by mass spectrum. After electrolysis, mass spectrometry showed that the catalyst still contained only organic ligands (m/z (M−H) = 197), whereas new structures were founded in the electrolyte (m/z (M + H) = 185 and 169). The ligand H$_4$dhbdc dissolved in the electrolyte solution. After O$_2$ was introduced into the solution, mass spectrometry identified a peak at m/z = 169 whereas another peak was found 1 day later at m/z = 185.[53] Compared with the H$_4$dhbdc ligands, the oxidation products possess a bent angle for the bridging ligand (Figure 6b). The electron-absorbing carbonyl group was applied to replace the electron-donating

hydroxyl groups. The smaller the bridging angle, the weaker the coordination ability, leading to the preferred escape of oxidized pillars from the layers. AFM showed that 2D-Co-NS had a thickness of ≈2 nm. Through electrolysis, 3D-Co@Ni formed by the direct growth of 3D-Co on the NF and further transformed into 2D-Co-NS@Ni. Further, an electrode modified by Fe-doped 2D-Co-NS (Fe:2D-Co-NS@Ni) was able to fabricate based on the immersion of 3D-Co@Ni, which shows a low overpotential of 211 mV (10 mA cm^{-2}) with a Tafel slope of 46 mV dec^{-1}.

Recently, 2-aminoterephthalic acid (NH$_2$-BDC) was selected as the organic ligand to synthesize 2D bimetal MOF (Co$_x$Fe-MOF) NSs, which satisfied the criteria for OER and nitrogen reduction reaction (NRR) concurrently.[54] By changing the mole ratio of Co/Fe, the 2D Co$_x$Fe-MOFs were fabricated in the precursor
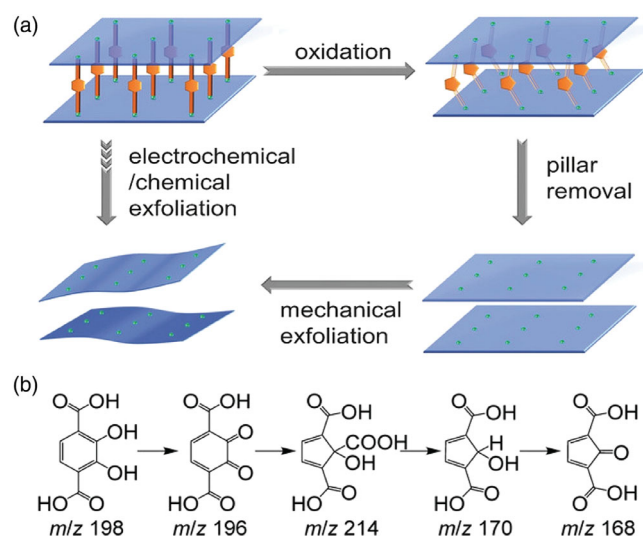
2000067 (11 of 31)

Figure 6. a) Schematic of selective pillar removal and exfoliation of a pillared-layer MOFs. b) A possible oxidative transform process from H_4dhbdc to a species with $m/z = 168$. (a,b) Reproduced with permission.[52] Copyright 2018, Wiley-VCH Verlag GmbH & Co. KGaA.

solution via the sonication synthesis method. A current density of $10 \, mA \, cm^{-2}$ was obtained from the Co_3Fe-MOF catalyst at an overpotential of 280 mV and a small Tafel slope of $38 \, mV \, dec^{-1}$ in the alkaline electrolyte. The excellent OER performance relies on the abundant active sites, as well as the significant contribution of metal-ion couplings. XPS results indicated the partial charge transfer from Fe to the center of Co, resulting in a larger electron density at the Co center. Co^{2+} and Fe^{2+} show the electronic configuration of $3d^7$ and $3d^6$, respectively, indicating a high electron filling of the e_g orbits in optimizing the electron fillings and increasing the catalytic activity for OER.[55] The introduced Fe ions not only modulate the valence state of Co^{2+} but also optimize the electron-accepting ability for OER, which further influences the coupling effect between metal ions in MOFs. The synergy effect of bimetals was considered to be the key to accelerating the OER process.[56]

Moreover, a fluorine-containing organic functional group (–F) was used in the electrocatalysis of 2D cobalt tetrafluoro-benzene-dicarboxylate CoTFBDC MOFs NS crystals (CoTFBDC).[57] 2D CoTFBDC MOF crystals were synthesized in a glass test tube following a bottom-up synthesis method. Moreover, the ultrathin graphite NS can be ultrasonically exfoliated from the liquid-phase graphite. Then, based on the codispersion method, scientists were able to form the heterostructure CoTFBDC/EG based on the combination of MOFs and exfoliated graphite (EG). Such a process needs to be conducted in the DMF to completely remove all the solvent from the heterostructure. CoTFBDC/EG-250 was obtained by heat treatment at 250 °C. The layered composites were prepared from two different 2D nanomaterials to promote electroactivity, which is beneficial from the strong interactions between electroactive F and Co atoms. The CoTFBDC/EG-250 exhibits the small Tafel slope of $39.8 \, mV \, dec^{-1}$. When introducing the Co-based MOFs with fluorinated organic ligands, the annealing results in the initial

decomposition of the structure. This process will stabilize the tiny CoF_2 nanocrystals on the support. However, F and Co separate at the higher annealing temperature. The double-layer capacitance (C_{dl}) of CoTFBDC/EG-250 was $4.68 \, mF \, cm^{-2}$, which was more than sixfold higher than that of the F-free CoBDC/EG composite. The electron paramagnetic resonance (EPR) results confirm the improved electron mobility in the structure, which leads to the enlarged electron spin relaxation rates of Co ions. Due to the effective electronic contact between the conductive EG support and the MOF nanocrystals, the introduction of F plays a significant role in achieving the optimal electron transfer between the electrolyte and the active metal surface. With such an electronic structure, excellent OER activity is expected.

2.3. Naphthalene-Based Dicarboxylate

Naphthalene-based dicarboxylate acid is also a common aromatic carboxylic acid ligand. Two carboxyl groups of 2,6-naphthalene dicarboxylate (NDC) are located on both sides of the naphthalene ring and have small steric hindrance. The stability of MOFs depends on their inherent frameworks, that is, the coordination metal ions, the hydrophobicity of organic ligands, and the coordination geometry of metal ligands.[58] 2,6-naphthalene dicarboxylate ligand with strong C–H–π interaction can be used as a rigid auxiliary ligand to effectively improve the structural stability of the MOFs.[59] Its coordination configuration is similar to that of BDC.

The bimetallic 2D CoNi-MOF nanoplate array with NDC as the organic ligand was grown directly on a copper foil (Cu substrate) by a simple hydrothermal process.[60] Different proportions of Co and Ni precursors were mixed with NDC to obtain different combinations of active sites (Co/Ni = 2:1, 1:1, and 1:2). SEM images showed petal-like and cubic structures for Co-MOFs and the Ni-MOFs. Meanwhile, the bimetallic MOFs prefer the formation of a 2D nanoplate array. The thinnest nanoplate array was obtained when the Co/Ni ratio reached 1:1. As the ratio of Co/Ni ratio varies, the thickness of the formed nanoplates also changes. CoNi(1:1)-MOFs show an overpotential of 265 mV and the Tafel slope was $56 \, mV \, dec^{-1}$ for the OER. The overpotentials of 301, 309, 341, and 375 mV were required for CoNi(1:2)-MOFs, CoNi(2:1)-MOFs, Co-MOFs, and Ni-MOFs at the current density of $10 \, mA \, cm^{-2}$, respectively. The excellent catalytic activity of 2D CoNi-MOFs was associated with the dominant (220) facets, which enhanced conductivity, thereby facilitating the transfer of electrons from the Cu substrate to the active catalytic centers. The smallest d-spacing from CoNi(1:1)-MOFs indicated that the structure has contracted, which induces an increased overlap contributing to the enhanced MOF conductivity by accelerating the transfer of electrons to the edge to improve the OER process at these sites.

Based on the same organic ligand, Duan et al. reported a strategy for growing ultrafine 2D MOFs NS arrays in situ on a variety of carriers.[23] A one-step chemical bath deposition method has been proposed for the synthesis, which relies on adding the organic ligand into the nickel acetate and iron nitrate solutions in the presence of the Ni foam substrate (**Figure 7**a). The crystal structure of the MOFs consisted of the alternating 2,6-naphthalene dicarboxylic group and inorganic metal–oxygen layers (MO_6 units; M = Fe, Ni or Cu). The NiFe-MOFs grown on Ni foam
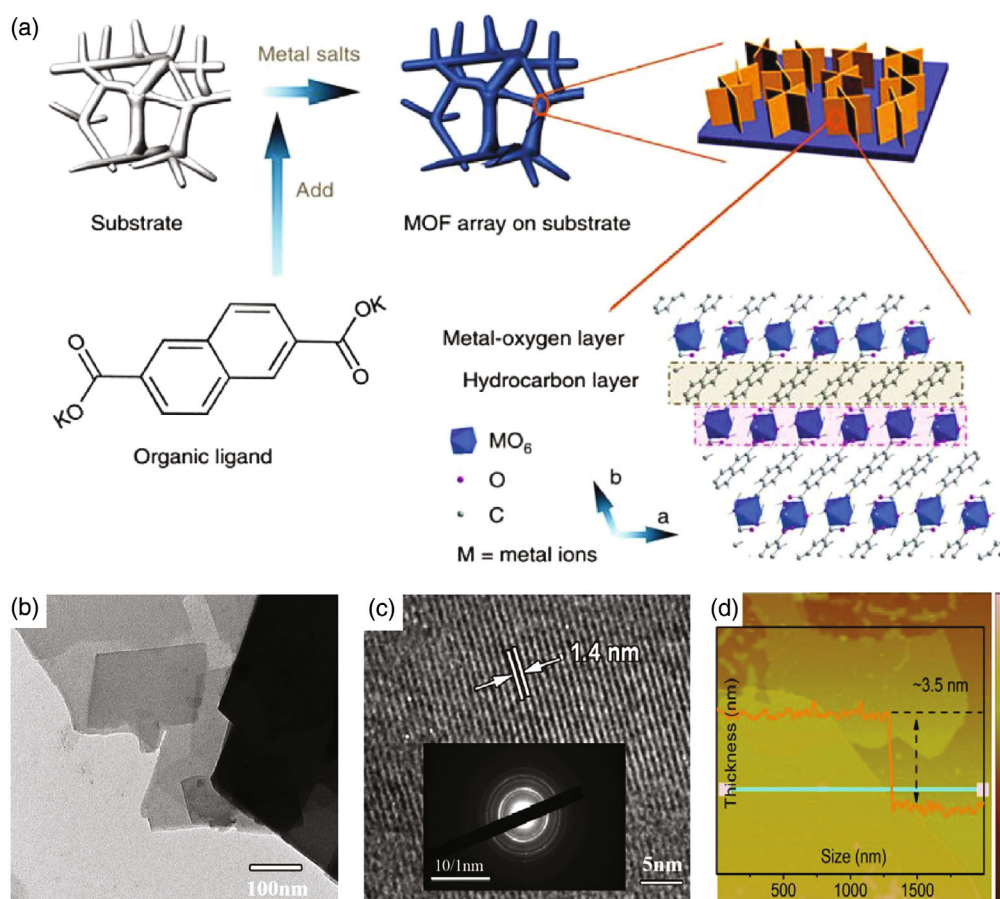
Figure 7. a) Synthetic process of MOF NS array; b) TEM image of NiFe-MOFs e; c) High resolution tunneling electron microscope (HRTEM) image and SAED pattern of NiFe-MOFs; d) AFM image and corresponding height profile along the marked green line of NiFe-MOFs electrodes. (a–d) Reproduced with permission.[23] Copyright 2017, Nature Publishing Group.

(NiFe-MOFs/NF) were a macroscopic NS array with high flexibility and the sizes of the structure can be easily modulated. The surface of the thin film was composed of a set of vertically grown NSs with a distance of tens of nanometers between adjacent layers (Figure 7b). These 2D MOF NSs had a well-defined crystalline structure, as shown by the clear lattice fringes in Figure 7c. The thickness of NiFe-MOF nanolayers was determined to be ≈3–5 nm by AFM (Figure 7d). The electrocatalytic performance of NiFe-MOFs for OER was tested in 0.1 M KOH solution in a typical three-electrode system. The overpotential of NiFe-MOFs was 240 mV at a current density of 10 mA cm^{-2}.

2.4. Dual Ligands

The microstructure differences significantly influenced the catalytic activity.[61] The coordination mode of dual ligands is more varied. The ratio of the two ligands in the MOFs can be simply changed to modulate the microstructure and further improve OER activity.[62] Moreover, dual ligands of various advantages can be selected to synthesize multifunctional catalysts. For example, Li and coworkers used BDC (A) and 2-aminoterephthalic acid (B) for the synthesis of heterogeneity MOFs (AB-MOF-

FeCo).[63] The OER activity of AB-MOF-FeCo was better than that of A-MOF-FeCo and B-MOF-FeCo synthesized with a single ligand. However, the similar catalytic activity between B-MOF-FeCo and A-MOF-FeCo supports a key factor of the mixed ligands. Due to the structural engineering regarding the metal node and ligands, the electronic structure of the intrinsic catalytic center in MOFs has been optimized, which further results in the excellent electrocatalytic performance for OER. After adding the ligand 2-aminoterephthalic acid (B) to bimetallic A-MOF-FeCo, the double-layer capacitance (C_{dl}) of AB-MOF-FeCo significantly increased, indicating more exposure of electrocatalytic active sites in AB-MOF-FeCo. The valence band maximum energy of AB-MOF-FeCo (1.22 eV) was lower than that of A-MOF-FeCo (1.32 eV) and B-MOF-FeCo (1.45 eV), demonstrating the optimized electronic environment induced by the ligand substitutions to support the faster electron transfer.

Recently, 2D Co-MOFs [Co(BDC)$_2$(SPDP)$_2$(DMF)(H$_2$O)] (SPDP = 4,4′-(sulfonylbis (4,1-phenylene))dipyridine) were used as the single-source precursors to afford the N-, O-, and S-tri-doped carbon matrix encapsulated with Co$_9$S$_8$ nanocomposites (Co$_9$S$_8$@TDC) through direct carbonization (**Figure 8**a).[64] Co$_9$S$_8$@TDC-600, -700, -800, and -900 were obtained by calcining the synthesized Co-MOFs at the different temperatures of 600,

ADVANCED
SCIENCE NEWS
www.advancedsciencenews.com

ADVANCED
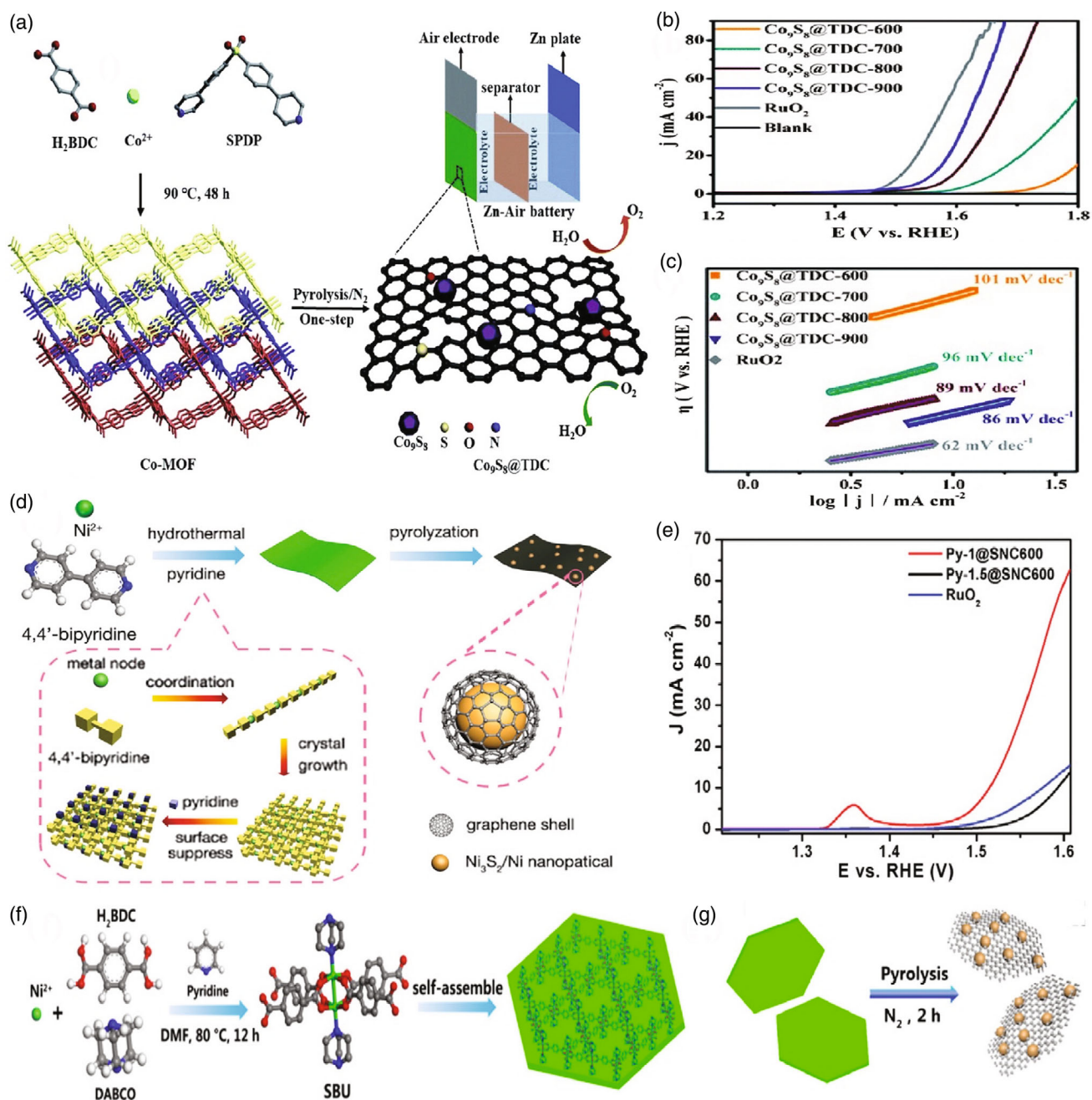**ENERGY & SUSTAINABILITY**
RESEARCH
Open Access
www.advenergysustres.com

Figure 8. a) Schematic illustration of the preparation procedure of Co_9S_8@TDC as bifunctional electrocatalysts. b) LSV curves of Co_9S_8@TDC nano-materials for OER in 1.0 M KOH; c) the corresponding Tafel curves. (a–c) Reproduced with permission.[64] Copyright 2019, Royal Society of Chemistry. d) Schematic of the synthesis strategy of 2D N-doped Ni-Ni_3S_2@carbon nanoplates from the Ni-based MOF precursor; e) LSV curves of Py-1@SNC600, Py-1.5@SNC600, and RuO_2. (d,e) Reproduced with permission.[66] Copyright 2019, Wiley-VCH Verlag GmbH & Co. KGaA. f) Schematic for the HXP preparation; g) Schematic for the pyrolysis process toward HXP@NC800. (f,g) Reproduced with permission.[67] Copyright 2020, American Chemical Society.

700, 800, and 900 °C, respectively. The heteroatom-doped carbon shell largely enhances the OER and ORR performances due to the protective effect. Co_9S_8@TDC-900 displayed an overpotential of 330 mV at a current density of 10 mA cm^{-2} for OER (Figure 8b,c). This excellent catalytic activity can be attributed to the unique structural advantages of the material, in which

more defects are formed in the structure under a higher pyrolysis temperature. Larger defects were conducive to improving the catalytic activity in OER and ORR.[65] The measured double-layer capacitance value of Co_9S_8@TDC-900 was 27.57 mF cm^{-2}. Therefore, the optimized material structure and electronic environment of Co_9S_8@TDC-900 guarantee high performance.

**ADVANCED
SCIENCE NEWS**
www.advancedsciencenews.com

**ADVANCED
ENERGY & SUSTAINABILITY
RESEARCH**
Open Access
www.advenergysustres.com

Using pyridine as an inhibitor, the Ni-based MOF nanoplate precursors with 2D morphology were obtained through the solvothermal method. Ni^{2+} and 4,4′-bipyridine were added in the water/ethanol mixed solvent with different concentrations (1 mL;1.5 mL) of pyridine. Then, N-doped Ni-Ni_3S_2@carbon nanoplates (Py-1@SNC600; Py-1.5@SNC600) annealed under inert gas protection (Figure 8d).[66] The Ni^{2+} cations extend to 1D chains via the 4,4′-dipyridine nitrogen connection. With the infinite chains stacked in parallel, the 2D cross-waved planes are noticed along the *c* axis. As the monodentate ligand inhibitor, the missing pyridine significantly hindered the crystal growth in the *c* direction, leading to the formation of 2D nanoplates. By changing the concentration of pyridine, it is possible to change the sizes of the nanoplates as well. However, the thickness will not be evidently changed by the increase in pyridine. The overpotential for Py-1@SNC600 was 284.7 mV at the current density of 10 mA cm^{-2} in 1.0 M KOH (Figure 8e). Moreover, Liu and coworkers used BDC and 1,4-diazabicyclo[2.2.2]octane (DABCO) for the synthesis of the 2D nickel-based MOF hexagonal nanoplate (HXP) (Figure 8f).[67] The HXP was prepared by a pyridine-assisted bottom-up method, in which a topological network was guided by the inhibition and modulation of pyridine. Nanorods (HXR) and nanodisks (HXD) were synthesized from different amounts of pyridine. Ni^{2+} was coordinated with oxygen atoms from carboxyl to form a paddlewheel secondary building unit, which is connected with the DABCO molecules by the terminal nitrogen atoms. In the preparation of N-doped Ni@carbon nanoplatelets (HXP@NC800), HXP was used as a precursor for annealing (at 800 °C for 2 h) with the protection of inert gas (Figure 8g). The overpotential of HXP@NC800 was 307 mV at a current density of 10 mA cm^{-2}.

2D Co-based MOF-on-MOF heterojunction nanostructures with improved OER activity were prepared via the two-step method, using 4,4′-biphenyldicarboxylate (BPDC) and BDC as ligands and Co^{2+} ions as the center atoms.[68] The 2D Co-BPDC nanostructures were obtained at room temperature by mixing Co^{2+} ion and BPDC ligand in the water/dimethyl sulfoxide (DMSO) solvent. Subsequently, to obtain Co-BPDC/Co-BDC heterojunction nanostructures, Co-BDC NSs were grown on the surface of Co-BPDC. XRD analysis indicated that when the Co-BPDC/Co-BDC formed, the BDC ligands first coordinated with Co atoms on the surface of Co-BPDC. Then, the BDC ligands reacted with Co ions in the solution to form Co-BDC. The overpotential of 2D Co-BPDC/Co-BDC was 335 mV at a current density of 10 mA cm^{-2}, which is much smaller than those of Co-BDC (392 mV), Co-BPDC (428 mV), and IrO_2 (346 mV).

2.5. N- and S-Heterocyclic Ligands

The organic heterocyclic ligands containing nitrogen, sulfur, and carboxylic acid coordination primitives are also the representative ligands for the preparation of 2D MOF materials. The researchers showed that the heteroatom-doped (especially N-doped) heterocyclic ligands can improve the catalytic activity.[69] Heteroatoms can be doped by heterocyclic ligands. Heteroatoms in different ligands bound to metals have different electrocatalytic activities due to the different ring structures of ligands.[70] The interfacial electron transfer of electrocatalysts

can be greatly promoted due to the high affinity of nitrogen to the transition metal ions.[71] Therefore, N-heterocyclic ligands are the most commonly used.

Recently, a new method was developed for improving OER performance. 2-methylimidazole (2MeIm) was selected as the organic ligand for the synthesis of Co-based 2D MOF NSs (Co-MOFs) on the carbon cloth (CC).[72] Subsequently, the 2D Co-MOF mesoporous structure of doped Fe with oxygen vacancies and unsaturated metal–oxygen sites was prepared on the CC substrate with O_2–Ar radio frequency (RF) plasma treatment (**Figure 9**a). Further carbonization was conducted to fabricate the optimum porous Fe/Co–carbon heterostructure (Fe_1Co_3/V_O-T, T = 700, 800, and 900 °C, Fe:Co atomic ratio of 1:3). The increased electrical conductivity and the uniform distribution of atoms facilitate the fast electron transfer within the framework. The Fe_1Co_3/V_O-T shows the porous structure (Figure 9b–d). Such mesoporous NSs demonstrate a much shorter electron transfer path with a higher transfer efficiency. The O_2–Ar RF plasma treatment further created oxygen vacancies, which largely modified the electronic structure of active sites to improve the OER performance. The excellent OER performance of Fe_1Co_3/V_O-800 in 1.0 M KOH has been determined with an overpotential of 260 mV at 10 mA cm^{-2} and a Tafel slope of 53 mV dec^{-1}, originating from the high concentration of vacancies and oxidized active metal sites. For comparison, the Co-MOF/V_O-800 catalyst was also procured without introducing Fe. Compared with Co-MOF/V_O-800, the 3D charge density of Fe_1Co_3/V_O-800 displayed charge accumulation after the introduction of Fe (Figure 9e,f). Meanwhile, the density of states (DOS) of Fe_1Co_3/V_O-800 also confirmed the higher electron density than that of Co-MOF/V_O-800 (Figure 9g), supporting a more efficient electron transfer to participate in the OER process. The adsorption energy of water has also been investigated to evaluate the electroactivity of catalysts, in which the water adsorption energies on Co-MOF/Vo-800 and Fe_1Co_3/V_O-800 are 0.62 and 0.81 eV, respectively (Figure 9h, i). These results showed that filling the oxygen vacancy with Fe atoms was helpful to modulate the metal active sites on the MOFs for the optimization of the electronic structure with a high concentration of active sites of the catalyst.

Based on the same organic ligand (2-methylimidazole), well-aligned cobalt MOF (Co-MOF) NSs were grown on 3D conductive Ni foams through a room-temperature solution-phase method. The nickel foam was added into the aqueous solution containing metal ions and organic ligands, stirred for 12 h.[73] Subsequently, the obtained Co-MOFs were converted into defect-rich ultrathin 2D $Co(OH)_2$ (D-U-$Co(OH)_2$) by an in situ etching treatment using ethanol solution containing cobalt chloride hexahydrate (pH = 5–6). The MOF layer did not easily form on the Ni foam in the first 6 h. So, the bare Ni foam was first immersed into the 2-methylimidazole aqueous solution overnight and then immersed into the mixed solution of Co^{2+} and 2-methylimidazole for 6 h; as a result, a uniform purple layer was observed on Ni foam. Therefore, it was believed that the 2-methylimidazole molecules were first adsorbed on the surface of Ni foam and then formed Co-MOFs by coordination with Co^{2+} ions in the aqueous solution. The overpotential of D-U-$Co(OH)_2$ required to reach a current density of 10 mA cm^{-2} was 236 mV before current and ohmic resistance correction and reduces to 223 mV after applying 90% current and ohmic resistance
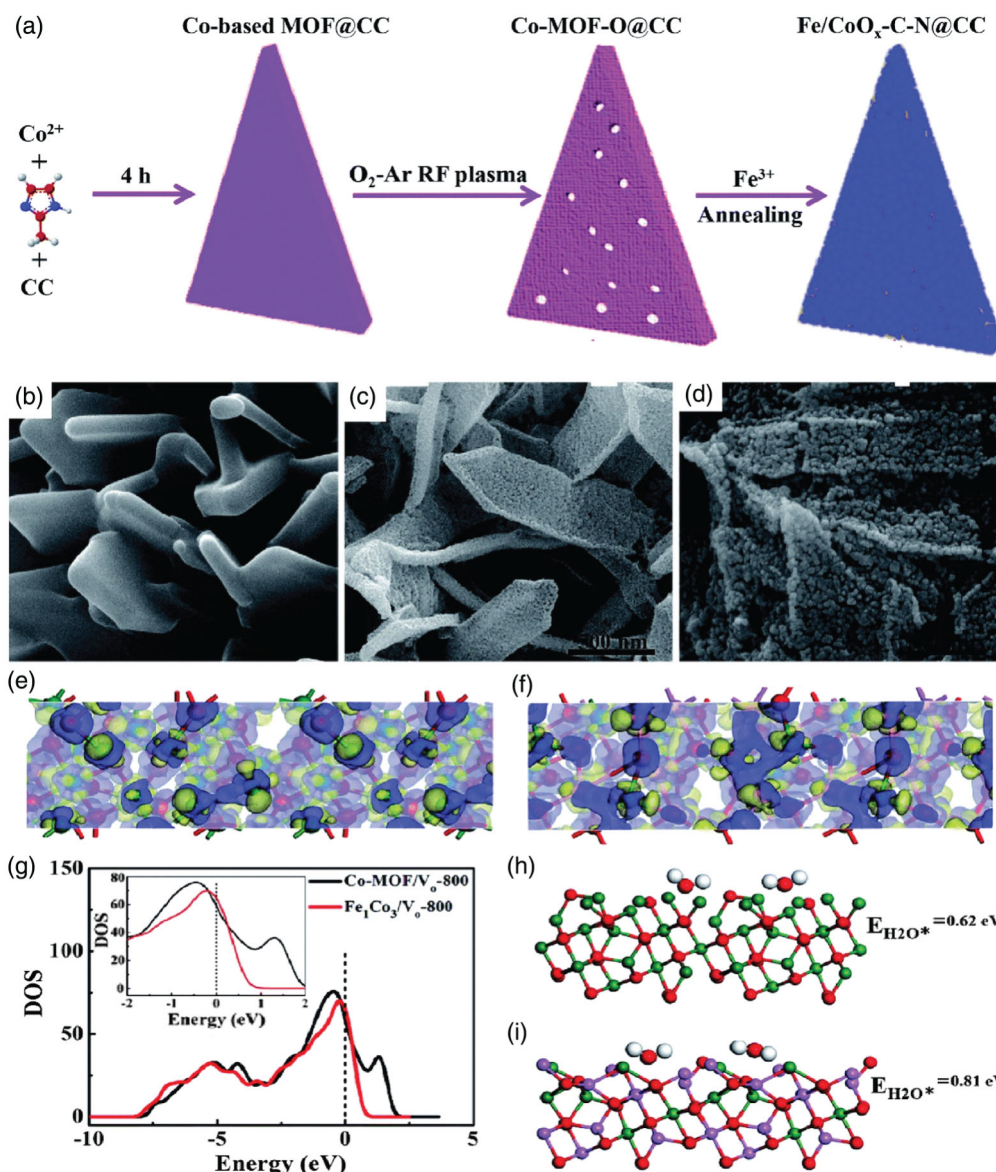
**ADVANCED
SCIENCE NEWS**

www.advancedsciencenews.com

**ADVANCED
ENERGY & SUSTAINABILITY
RESEARCH**
Open Access

www.advenergysustres.com

Figure 9. a) Schematic illustration of the preparation process of porous Fe/Co–carbon with a microstructure inspired by triangular-shaped cheese; b) SEM image of original Co-MOF@CC; c) SEM image of Co-MOF@CC modified by O_2–Ar RF plasma at 180 W; d) SEM image of Fe_1Co_3/V_O-800; e) 3D charge distributions of Fe_1Co_3/V_O-800; f) 3D charge distributions of Co-MOF/V_O-800; g) the DOS; and water adsorption energies for h) Fe_1Co_3/V_O-800 and i) Co-MOF/Vo-800. (a–i) Reproduced with permission.[72] Copyright 2019, Royal Society of Chemistry.

correction. In addition, the onset potential of D-U-Co(OH)$_2$ was about ≈1.39 V.

Co-MOF with a unique crystalline structure was synthesized using 4,5-Imidazoledicarboxylic acid as an organic ligand, in which the central metal interacted with nitrogen and oxygen atoms from the H_2O molecules and organic ligands.[74] After removing the H_2O molecules through the facial method, more active metal sites are exposed to improve the chemical activity.[75] The results showed that electroactivity significantly increased sevenfold by the introduction of Fe, attributed to the modulation bonding strength between the central metal sites and surrounding coordinated water molecules. After electrochemical activation, the 2D amorphous structure of CoFe-MOF-OH is still

preserved. DFT calculations showed that the electronic structures of Co sites in CoFe-MOF have been modulated, which changed the adsorption strength of intermediates. Both CoFe-MOF and Co-MOF show the metallic feature with the DOS close to the Fermi level.[76] Moreover, the strategy of bimetal MOF leads to the formation of a delocalized and an upshifted d-band in the Fe state toward the Fermi level, indicating that the electroactivity of CoFe-MOF remarkably improves by Fe incorporation (**Figure 10**a).[46c,77] The Co atom in CoFe-MOF has slightly lower 3d electrons than Co-MOF, which are both higher than the theoretical estimation (Figure 10b). The free energy diagram of electrocatalysis identified that the RDS of CoFe-MOF and Co-MOF result from the conversion from *OH to O*. With the introduced
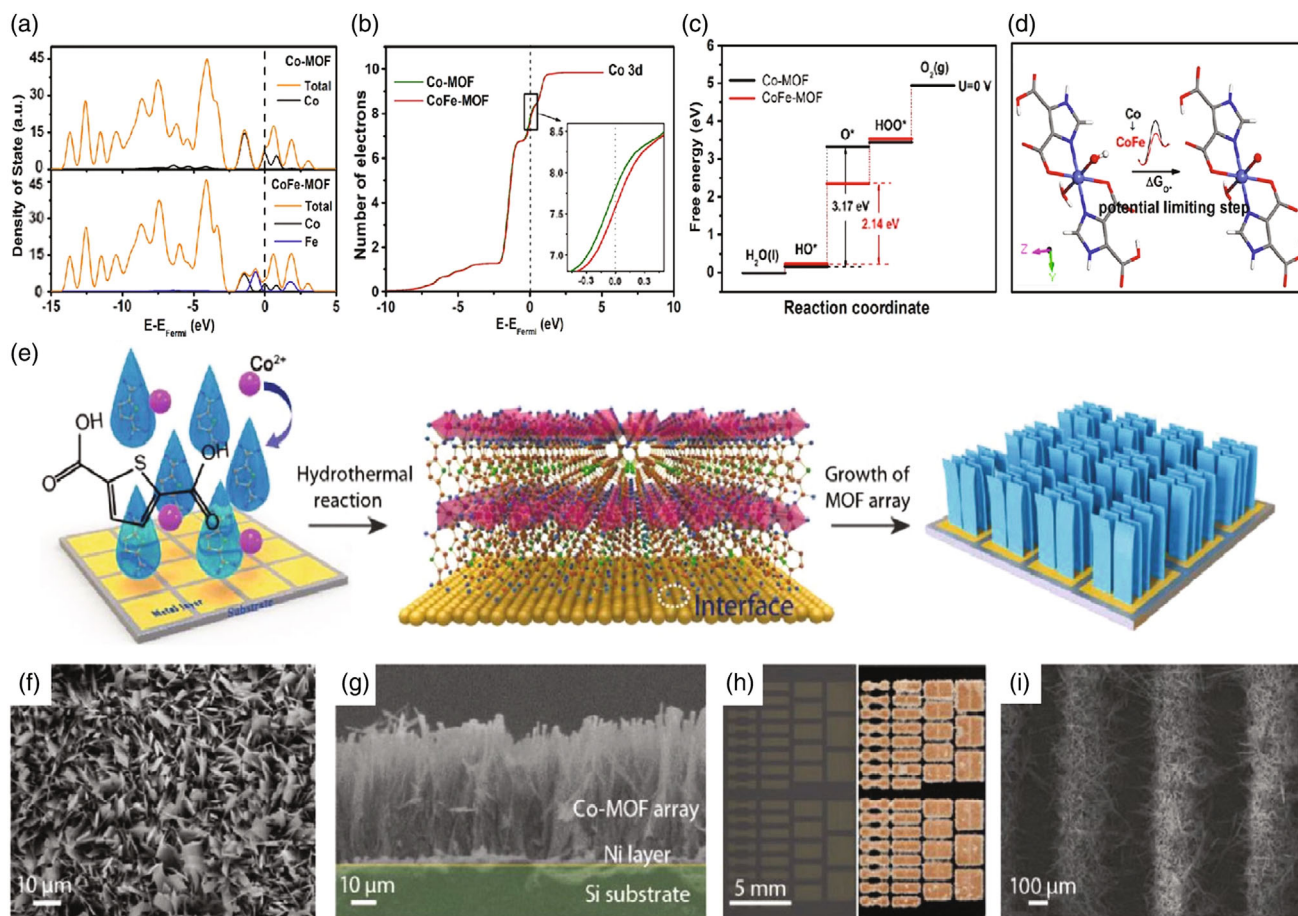
Figure 10. a) DOS of CoFe-MOF and Co-MOF; b) the Number of 3d electrons of MOF; c) standard free energy diagram of CoFe-MOF and Co-MOF for the OER process; d) potential limiting step model of OER catalysis. (a–d) Reproduced with permission.[74] Copyright 2019, American Chemical Society. e) Schematic of the growth of Co-MOF nanoarrays on a thermally evaporated metal layer, allowing the patterning of nanoarrays and the independence of growth on the underlying substrates. f) SEM image of the top view of the Co-MOF nanoarrays grown on the Ni-coated silicon substrate; g) cross-sectional SEM image of Co-MOF nanoarrays; h) optical images of patterned Ni layers on the Si substrates before (left) and after (right) the growth of the Co-MOF nanoarrays; i) SEM image of the growth of the Co-MOF nanoarrays on the patterned Ni layers. (e–i) Reproduced with permission.[79] Copyright 2019, Wiley-VCH Verlag GmbH & Co. KGaA.

Fe, the energy barrier of the RDS was obviously lowered (Figure 10c,d). CoFe-MOF exhibited a lower overpotential (351 mV) at a current density of $10 \, \text{mA} \, \text{cm}^{-2}$ with a smaller Tafel slope ($44 \, \text{mV} \, \text{dec}^{-1}$) than that of Co-MOF, demonstrating an improved OER efficiency. Furthermore, 2D Co-based bimetallic MOFs (Co-Fe/Ni@HPA-MOF NSs) were synthesized by the in situ hydrothermal ($130 \, ^\circ\text{C}$ for 4 days) synthesis with hypoxanthine (HPA) as the organic ligand.[78] The electrocatalytic activity was investigated in 1.0 M KOH solution. Co-Ni@HPA-MOF shows an overpotential of 320 mV to realize the current density of $10 \, \text{mA} \, \text{cm}^{-2}$ with a Tafel slope of $58 \, \text{mV} \, \text{dec}^{-1}$ to support high kinetics for electrocatalysis.

Recently, Wang et al. have reported the high directional growth of ultralong quasi-2D MOF nanoarrays through the delicate utilization of the thermally evaporated metal layer.[79] The growth of Co-MOF nanoarrays has been investigated on Si or glass, where the substrates were submerged in the mixed solution under hydrothermal conditions (Figure 10e). To promote the growth of nanoarrays, Ni coating is needed to realize the

fully covered high-density Co-MOFs nanoarrays, which display the vertical growth direction of quasi-2D nanobelts. However, the thickness of Ni coatings did not affect the growth (Figure 10f,g). The introduction of Ni coatings is highly necessary to facilitate the growth of MOF nanoarrays, where the selectivity applies to control the growth of the localized nanoarrays (Figure 10h). The growth has been selective on the surface. Without metal coating, there would be no growth on silicon or glass slides (Figure 10i). From the SEM and AFM image characterizations, the thicknesses of nanobelts are estimated to be ≈100 nm. Therefore, Co-MOFs nanoarrays on the Ni foam (Co-MOF/NF) show the highest OER performance. This is attributed to the fast ion and electron conduction efficiency in the porous conducting substrates. Meanwhile, other metal-coated substrates can also enhance OER performance. The Co-MOF/NF exhibited OER activity with an overpotential of 270 mV at the current density of $10 \, \text{mA} \, \text{cm}^{-2}$, surpassing most Co-based or MOF-derived electrocatalysts discussed in previous works.

The S-doped heteroatom could regulate the adsorption of reaction intermediates and thus improve the catalytic activity.[80] The preparation of Cu_2O-based composite arrays (2D Cu_2O-C_{TDC}) was also based on H_2TDC.[40] A series of 2D Cu-based MOF derivatives were fabricated by the pyrolysis of the 2D Cu-TDC, Cu-FDC (FDC = 2,5-furandicarboxylate), and Cu-BDC arrays, respectively. Cu_2O/C_{FDC} and Cu_2O/C_{BDC} show the normal overpotentials of 352 and 360 mV, respectively, which are much lower than the 3D Cu_2O/C_{BTC}, bare Cu_2O, and Cu_2O/S-C_{TDC}. The Tafel slope was compared in the order as was Cu_2O/S-C_{TDC} (65.6 mV dec^{-1}) < Cu_2O/C_{BDC} (84.7 mV dec^{-1}) < Cu_2O/C_{FDC} (86.2 mV dec^{-1}) < Cu_2O/C_{BTC} (105.4 mV dec^{-1}) < Cu_2O (125.1 mV dec^{-1}). Moreover, the 2D Cu_2O/S-C_{TDC} arrays show a much larger specific surface area of 160.4 m^2 g^{-1} than Cu_2O/C_{BDC} and Cu_2O/C_{FDC}. The calculated C_{dl} value also confirmed the results. These results indicate that the potential formation of the defect matrix and structure change are induced by S doping, which is highly useful for promoting higher conductivity.[80,81]

2.6. Phthalocyanine- and Porphyrin-Based Ligands

Phthalocyanine and porphyrin organic ligands have good stability due to their rigid structure. Therefore, phthalocyanine- and porphyrin-based MOFs materials generally have better stability. The N atoms in the phthalocyanine ring and porphyrin ring can combine with different metals to form metallophthalocyanine and metalloporphyrin, and it has good atomic utilization. DFT calculations how that the high activity of the material was attributed to the strong electronegativity of the nitrogen atoms, which modulated the electron cloud density of adjacent atoms and formed the active sites to promote the adsorption of the reactants.[82] Redox-active N4 macrocyclic materials have abundant electrochemical activity.[83] The large ring can also connect to various functional groups, which coordinates with metal ions to form more active sites.[84,85]

Based on the bottom-up strategy, the noble-metal-free nickel phthalocyanine-based 2D MOF (NiPc-MOF) has been reported in the experimental synthesis (**Figure 11**a).[84] The building block is 2,3,9,10,16,17,23,24-octaamino-phthalocyaninato nickel(II)(NiPc–NH$_2$), which is treated with NiCl$_2$ to form NiPc–NH$_2$. Subsequently, NiPc–NH$_2$ monomers were connected by reacting them with Ni(isq)$_2$ ligands (bis(o-diiminobenzosemiquinonate) nickel(II) to achieve NiPc-MOF as a huge π-conjugated 2D MOF with fourfold symmetry (Figure 11b). Next, different substrates can supply the growth platform for the NiPc-MOF material including fluorine-doped tin oxide (FTO), indium tin oxide (ITO), quartz glass, and silicon wafer. SEM images confirmed the thickness of 300 nm for the NiPc-MOF film on FTO with the catalyst loading of ≈7.6 µg cm^{-2} based on the inductively coupled plasma-atomic emission spectrometer (ICP-AES) results. For water oxidation, NiPc-MOF exhibited the onset potential at 1.48 V in the alkaline environment, representing an overpotential of ≈250 mV. This performance is superior to the most reported noble-metal-free OER catalysts.[86] In sharp contrast, the monomer 2,3,9,10,16,17,23,24-octatosylamido phthalocyaninato nickel(II)(NiPc-NHTs) and the blank FTO show a much higher onset potential for OER than

NiPc-MOF. In addition, NiPc-MOF showed a 30-fold higher mass activity of 883.3 A g^{-1} in the alkaline environment than that of the RuO$_2$.[87]

The cobalt NPs embedded in mesoporous N-doped graphitic carbon materials (Co@NC-800) were synthesized by carbonization procedures using Co-based porphyrin paddlewheel framework-3 (PPF-3)[88] 2D MOF NSs as a sacrificial template.[89] Co-P@NC-800 was derived through subsequent phosphorization of Co@NC-800. The SEM image showed a lateral size of ≈1.5 µm with the square-sheet crystals of PPF-3. The thickness is about 50–100 nm, and Co@NC-800 includes broken and wrinkled particles after carbonization. After extensive grinding and subsequent phosphorization treatment, the morphology of Co-P@NC-800 was well preserved compared with that of Co-P@NC-800. Co-P@NC-800 material exhibited good electrocatalytic properties with overpotentials of 98 and 370 mV and Tafel slopes of 74 and 79 mV dec^{-1} for HER and OER in acidic and alkaline electrolytes, respectively. Such performances are comparable with the best nonprecious metal water-splitting catalysts. In addition, an ideal precursor of the bimetallic porphyrinic MOF (Co-CuTCPP)/reduced graphene oxide (Co-CuTCPP/rGO) composite has been prepared by ultrathin porphyrinic MOF (Co-CuTCPP) NSs loaded onto graphene oxide (GO) via a hydrothermal process.[90] The TEM image revealed that the NSs of Co-CuTCPPMOF were well coated on the surface of rGO NSs with 1–2 layers, indicating that the heterojunction is formed between the Co-CuTCPPMOF and rGO sheets.

2.7. Advanced Synthesis of MOF-Derived Electrocatalyst

Besides directly applying the MOF materials for OER electrocatalysis, the MOF has also demonstrated a potential template to fabricate the layered double hydroxide (LDH) with special morphology, which is a highly promising electrocatalyst for OER. Lou and coworkers have reported a facile one-pot self-templated strategy based on spindle-like particles of MIL-88A to fabricate the Ni–Fe double-shelled nanocages (DSNCs), which are constructed by the self-assembly of the ultrathin NS.[91] In this work, by tailoring the volume ratios of the solvents, the number of the shell layer can be flexibly controlled. Due to the effect of simultaneous etching and coprecipitation, the obtained Ni–Fe LDH DSNCs exhibit the hierarchical hollow structure, which displays significantly improved electroactivity for the OER. MIL-88A possesses a smooth surface, which is the sacrificial template for the hydrolysis reactions to obtain the nanocage morphology. After the growth of the Ni–Fe LDH DSNCs is accomplished, MIL-88A is gradually etched by the hydrolyzation reaction. Meanwhile, through the coprecipitation of Fe species, Ni^{2+}, and OH$^-$ ions, the shell number is easily modulated by the speed of etching and coprecipitation. The obtained Ni–Fe LDH DSNC reaches 20 mA cm^{-2} with 246 mV overpotential and a Tafel slope of 71 mV s^{-1} for the OER process under the alkaline environment. The high stability of over 50 h is also achieved.

Recently, Huang, Tang, and Yan and coworkers also reported a significant advance in the fabrication of the Ni–Fe LDH nanocapsule by an ingenious one-step method based on the Ce doping strategy in MIL-88A.[92] The nanocapsule structures usually have a modifiable shell, high exposed surface area, and large
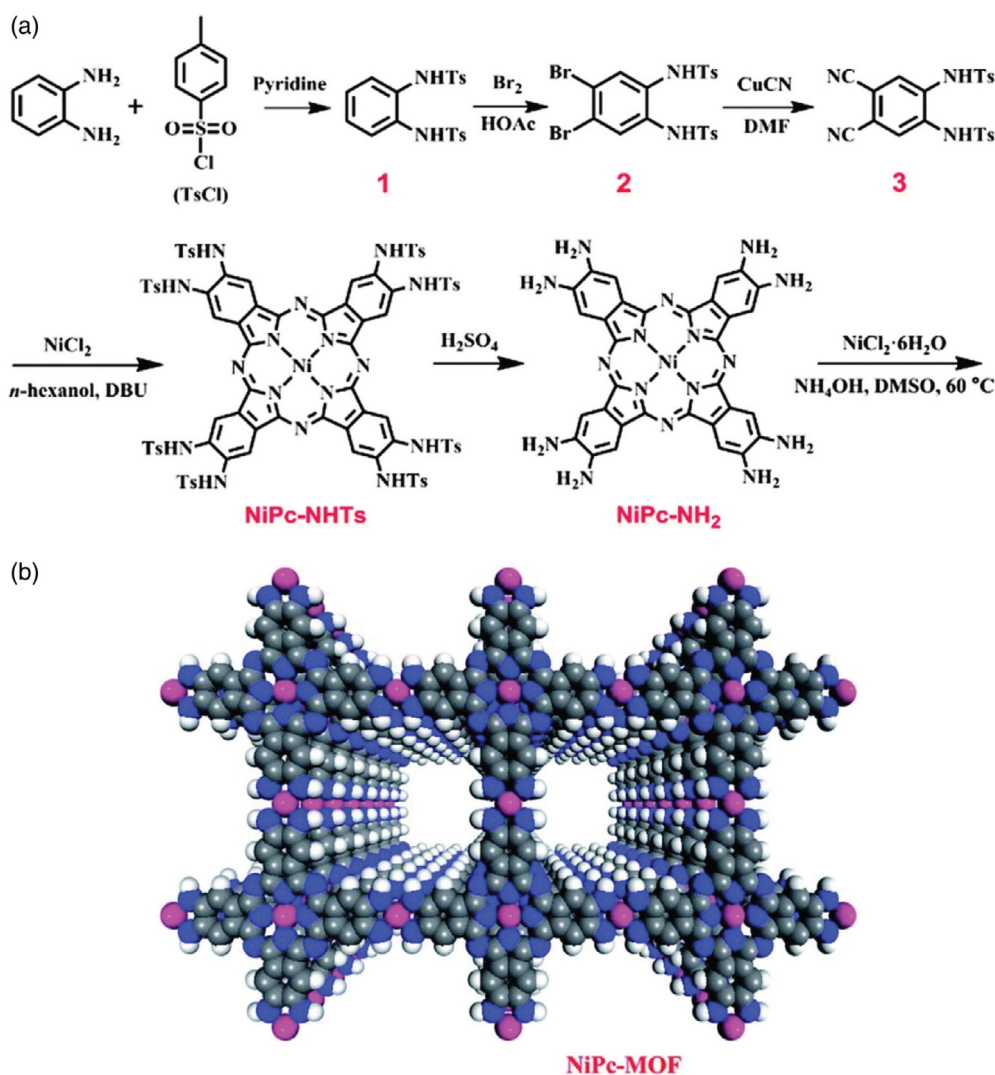
Figure 11. a) Chemical synthesis route for the NiPc-MOF; b) structure of the NiPc-MOF. (a,b) Reproduced with permission.[84] Copyright 2018, Royal Society of Chemistry.

accommodation space, which are highly beneficial for boosting the electroactivity of OER. However, the conventional synthesis for such structures usually requires complicated procedures with limited controllability. By introducing Ce doping, the crystalline phase of MIL-88A was effectively regulated and stabilized, leading to the synthesis of Ni–Fe LDH nanocapsule (**Figure 12**a). Such a strategy relies on the flexible valence states and high oxyphilic coordination ability of Ce, which facilitates tight binding with oxygen ligands in MIL-88A. More importantly, these tight bindings are able to resist the alkaline media and alleviate the metal–ligand bond dissociation issue. The obtained Ni–Fe LDH demonstrates 242 mV overpotential at the current density of 20 mA cm^{-2} for over 24 h. The extremely small Tafel slope of 34 mV s^{-1} for the OER process surpasses the commercial OER catalyst Ir/C (61 mV s^{-1}) and normal NiFe LDH (59 mV s^{-1}) (Figure 12b,c). After comparison, the Ce doping concentration of 30% exhibits the best electrochemical performance. Theoretical calculations have been introduced to investigate the

influence of Ce doping on the MIL-88 A and the OER performance. It is noted that Ce doping is energetically favorable at the pore structure in MIL-88A, which prefers forming stable bonding with nearby O and stabilizes the structure to synthesize the Ni–Fe LDH nanocapsule (Figure 12d). The facile structural transformation and enhanced OER process are ascribed to the electronic modulation by the d–f coupling with the Ce introduction (Figure 12e).

3. 2D MOFs for ORR

ORR is the key half reaction in fuel cell applications.[93] In the ORR process, the reduction of oxygen occurs either by a two-electron pathway (H_2O_2 or HO_2^-) or by a four-electron pathway (H_2O or OH^-)[94] Generally, the four-electron pathway is preferred due to the higher reaction kinetics and efficiency. The reaction mechanisms of ORR processes are also demonstrated below.
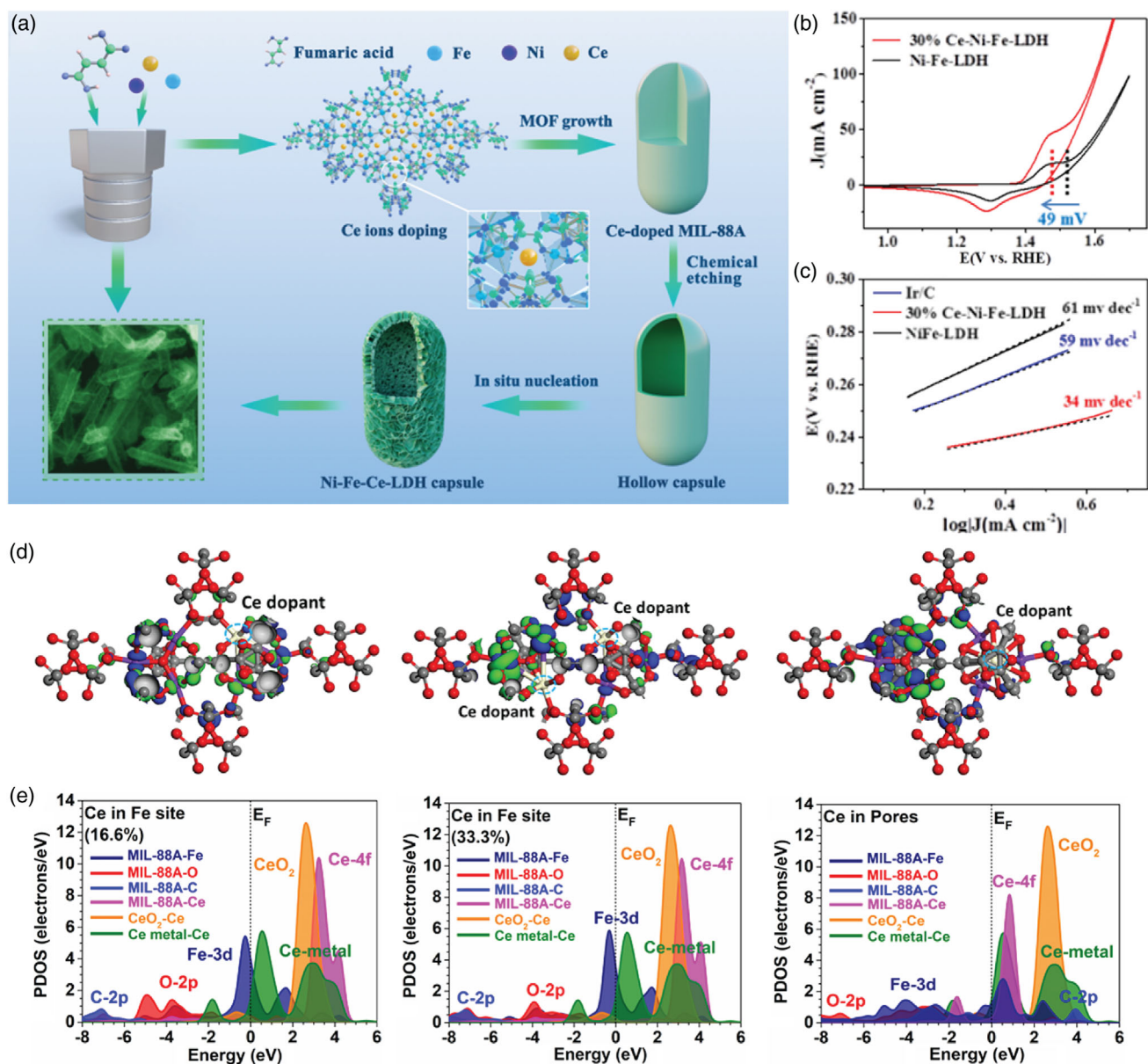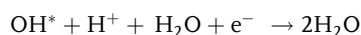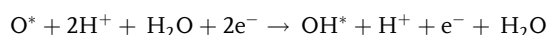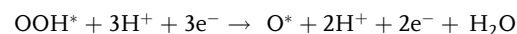
ADVANCED
SCIENCE NEWS

www.advancedsciencenews.com

ADVANCED
ENERGY & SUSTAINABILITY
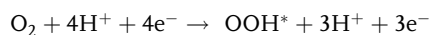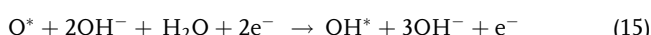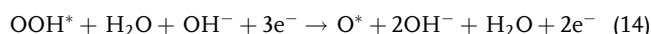RESEARCH
Open Access

www.advenergysustres.com

Figure 12. a) Schematic illustration of the fabrication of hollow Ni–Fe–Ce–LDH microcapsules mediated by cerium doping MIL-88A. b) Cyclic voltammetry curves of Ni–Fe–LDH and 30%Ce–Ni-–Fe–LDH. c) The Tafel slopes of Ir/C, Ni–Fe–LDH, and 30% Ce–Ni–Fe–LDH. d) The top view of the real spatial 3D orbital contour plots with Ce doping concentrations of 16.6%, 33.3% in Fe sites, and Ce doping in the pores of MIL-88A. e) The PDOS of Ce-doped MIL-88A of 16.6% concentration, 33.3% concentration, and the PDOS of Ce dopants in the pores within MIL-88A. Reproduced with permission.[92] Copyright 2020, Royal Society of Chemistry.

For the acidic solution

$$O_2 + 4H^+ + 4e^- \rightarrow OOH^* + 3H^+ + 3e^- \tag{9}$$

$$OOH^* + 3H^+ + 3e^- \rightarrow O^* + 2H^+ + 2e^- + H_2O \tag{10}$$

$$O^* + 2H^+ + H_2O + 2e^- \rightarrow OH^* + H^+ + e^- + H_2O \tag{11}$$

$$OH^* + H^+ + H_2O + e^- \rightarrow 2H_2O \tag{12}$$

For the alkaline solution

$$O_2 + 2H_2O + 4e^- \rightarrow OOH^* + H_2O + OH^- + 3e^- \tag{13}$$

$$OOH^* + H_2O + OH^- + 3e^- \rightarrow O^* + 2OH^- + H_2O + 2e^- \tag{14}$$

$$O^* + 2OH^- + H_2O + 2e^- \rightarrow OH^* + 3OH^- + e^- \tag{15}$$

$$OH^* + 3OH^- + e^- \rightarrow 4OH^- \tag{16}$$

**ADVANCED
SCIENCE NEWS**
www.advancedsciencenews.com

**ADVANCED
ENERGY & SUSTAINABILITY
RESEARCH**
Open Access
www.advenergysustres.com

The scaling correlation between *OH and O* adsorptions has been applied to the Pt-based catalysts and many other catalysts. Meanwhile, the volcano plot has demonstrated the development direction for optimal electrocatalysts. At present, Pt-based materials are still the most ideal ORR electrocatalysts in practical applications. However, the scarcity, high cost, and low durability of Pt limit its widespread use in these renewable energy technologies.[94,95b] Due to these limitations, the development of alternative energy materials with high activity and durability and abundant earth resources is a crucial and challenging task. Therefore, designing and synthesizing novel electrocatalysts to break the scaling correlation with high catalysis efficiency are the most urgent demands. To design the novel electrocatalysts, there are several strategies to follow based on the previous efforts in both experimental and theoretical calculations, which are similar to the OER electrocatalysts. First of all, the intrinsic catalytic activities of materials should be improved based on the appropriate nanoengineering in both the morphology and the defect/dopant control. Then, the concentration of active sites should be guaranteed to promote sufficient electron transfer. Moreover, mass transportation and electron conductivities are also critical prerequisites.

2D MOF is a new kind of porous material with good crystallinity and long-range order.[24c] 2D MOFs were rarely used directly as an ORR electrocatalyst. However, the 2D MOFs can be treated to obtain carbon-based ORR electrocatalysts with heteroatom doping, large surface area, and high conductivity.[96] In recent years, 2D MOFs for electrocatalytic ORR usually show nitrogen-containing ligands (e.g., 2-methylimidazole, benzimidazole, phthalocyanine-based, porphyrin-based, etc.), attributed to the high activity, remarkable stability, low cost, and being free from the methanol-crossover effect of the transition metal/N-doped carbon composites (M–N–C).[17,97] In the M–N–C structure, doping N into C can facilitate the ORR performance due to the electronegativity difference between C and N, and the positively charged C atoms are beneficial to oxygen adsorption and further enhance the ORR performance.[98] Here, we have classified the recently synthesized organic ligands of 2D MOFs for ORR into N-heterocyclic ligands, phthalocyanine and porphyrin ligands, and carboxylic acid donor ligands. This section introduces the synthesis strategy, compositions, morphologies, electrocatalytic performances, and reaction mechanisms of 2D MOFs-based ORR electrocatalysts. **Table 2** shows various 2D MOFs as electrocatalysts for ORR along with their ORR activities.

3.1. N-Heterocyclic Ligands

At present, the main N-heterocyclic ligands used in the synthesis of 2D MOFs in electrocatalytic ORR are 2-methylimidazole (2MeIm) and benzimidazole. The transition metal is coordinated with the nitrogen atom on the imidazole ring. The MOFs fabricated based on 2MeIm leads to a 3D structure, such as the well-known zeolite imidazolate frameworks (ZIFs). However, in recent years, ZIF NSs with 2D crystal structures and 2D shapes were synthesized by simple solvent replacement and salt template assistance.[99,100] Due to the large surface areas, 2D MOFs usually expose more active sites, which are
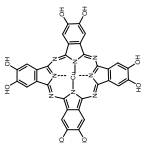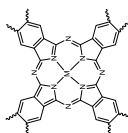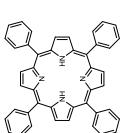
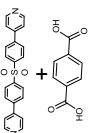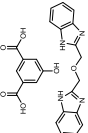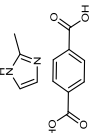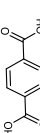advantageous than the 3D MOFs.[26,101] In addition, the N atoms in the N-heterocyclic ligand coordination form M–N_x with transition metal ions, which have been identified as active sites for ORR.[102] After further carbonization of the MOFs synthesized with N-heterocyclic ligands, N 1s XPS spectra showed the presence of pyridinic N, pyrrolic N, and graphitic N.[103] Previously, the results showed that graphitic N could greatly increase the catalytic current of ORR and pyridine N boosts the ORR on the N-rich carbon surface.[104]

To fabricate ultrathin ZIF-67 NS and carbonized Co,N-doped nanoporous carbon NS (Co,N-C NS) electrocatalysts, the salt template and calcination strategies have been proposed (**Figure 13**a).[99] With the salt template, $CoCl_2$ and 2MeIm in the methanol solution NaCl powder were mixed for pyrolysis at different temperatures ($T = 600, 700, 800,$ and $850\,°C$). The produced CoN_x, pyridinic-N, and graphitic-N play as the active species. These species are major catalytically active sites for ORR.[105] The appropriate solvent volume and precursor-to-salt ratio were the two most important requirements for the synthesis. After the slow evaporation of the methanol solvent, based on in situ pyrolysis, the NaCl@ZIF-67 NSs are converted into Co and Co,N-C NSs in the N_2 atmosphere, which show a large number of graphitic carbon nanopores in the structure. The origins of the porous structure and the graphitic carbon depend on the high-quality crystallization and the removal of Co species. The E_{onset} of Co,N-C NS-800 °C and Pt/C was 0.938 and 0.945 V, respectively. Moreover, the Co,N-C NS-800 °C also exhibited a more positive $E_{1/2}$ than Pt/C.

Through the two-step dimensional-reduction strategy, the ultrathin N-doped graphene nanomesh (NGM) is achieved, where the 2D Zn-based ZIF (Zn-ZIF-L) crystal structures are utilized as the precursors,[100] which show a leaf-like shape with a thickness of ≈ 160 nm (Figure 13a). Within inert atmosphere, the metal chlorides (LiCl/KCl) as the exfoliators and etching agents have been applied to exfoliate Zn-ZIF-L to form the ultrathin 2D NGM (Figure 13b). The best NGM is nanometer thin with a high specific surface area of 1329.5 $m^2\,g^{-1}$, N-doping concentration of 4.68 at %, and a hierarchical porosity level (Figure 13c,d). The XRD pattern shows the layered crystal structure of Zn-ZIF-L.[106] To study the temperature influence, thermal stripping was conducted at 700–900 °C to prevent weightlessness (NGM-x ($x = 700, 800, 900$). For comparison, Zn-ZIF-L was directly carbonized at 800 °C to obtain N-doped porous carbon (NC-L-800), which possesses a leaf-like structure with a largely increased specific surface area to 1329.5 $m^2\,g^{-1}$, originating from the insertion of metal ions (K^+) into Zn-ZIF-L to obtain a larger specific surface area. This interaction with carbon atoms produces more mesopore and micropores. Furthermore, the decreased microporous structure, specific surface area, and total pore volume originate from the over-exfoliation issue especially at high temperatures. As metal-free carbon-based electrocatalysts, NGM-800 displays an impressive ORR activity with E_{onset} of 0.860 V, $E_{1/2}$ of 0.781 V, and j_d of 4.243 mA cm^{-2}.

In addition, Co/Zn-containing bimetallic ZIF nanoleaves (Co_xZn_{1-x}-ZIF nanoleaves, x represents the molar ratio of $Co^{2+}/(Co^{2+} + Zn^{2+})$ in the original ZIF nanoleaves) were prepared by the shape-transforming method in an aqueous solution with 2-methylimidazole (2MeIm) as organic ligands.[99]

Table 2. List of 2D MOFs reported as electrocatalysts for ORR in 0.1 M KOH solution.

Ligand structure	Ligand name	Catalyst	Synthetic method	E_{onset}[V]	$E_{1/2}$ [V]	j_d [mA cm^{-2}]	Tafel plot	Electron transfer number [n]	Loading amount [mg cm^{-2}]	Ref.
2-methylimidazole(2MeIm)	Co,N-C NS-800 °C	Bottom-up	0.938	0.869	N.A	50.5	3.9	0.4	[97]
	NGM-800	Hydrothermal	0.973	0.886	4.828	N.A	3.85	0.25	[98]
	Co$_{0.6}$-N/C-800	Shape-transforming method	0.916	0.825	5.2	77	3.9	0.254	[99]
Benzimidazole(HBIM)	Co@Co$_3$O$_4$@C-CM	Solvothermal	0.93	0.81	N.A	N.A	3.8–3.9	0.1	[100]
	Co@FLG-40	Bottom-up	N.A	0.824	6.42	56	3.8	0.4	[126]
2,3,9,10,16,23,24-octahydroxyphthalocyaninato copper (PcCu-(OH)$_8$)	PcCu-O$_8$-Co/CNTs	Solvothermal	N.A	0.83	5.3	60	3.93	0.48	[127]
Metal phthalocyanines (Pc(M))	CAN-Pc(Fe/Co)	Heated in a muffle furnace	1.04	0.84	5.23	54	3.94	20 µg cm^{-2}	[9b]
Meso-Tetraphenylporphine (TPP)	COP-TPP(Fe)@MOF-900	Solvothermal	0.99	0.85	N.A	68	3.95	0.2	[16b]
Terephthalic acid; 4,4'-(sulfonylbis(4,1-phenylene))dipyridine(SPDP)	Co$_9$S$_8$@TDC-900	Solvothermal	1.50	0.78	5.45	86	3.94	1.7	[64]
5-hydroxyisophthalic acid(Hbbop); 2,2'-(oxybis(methylene))bis(1H-benzo[d]imidazole)(HO-BDC)	Co$_3$O$_4$@N/C	Hydrothermal	0.90	0.80	5.36	80	3.73	1.40	[110]
2-methylimidazole(2MeIm);1,4-Benzene dicarboxylic acid(BDC)	NiCo-NC	Sonication	1.038	0.866	N.A	86	3.90	0.3	[97a]
1,4-Benzene dicarboxylic acid(BDC)	Pt3.2%@NiNSMOFs	Ultrasonication	1.024	0.863	N.A	78	3.96	0.1	[114]

**ADVANCED
SCIENCE NEWS**

www.advancedsciencenews.com

**ADVANCED
ENERGY & SUSTAINABILITY
RESEARCH**
Open Access
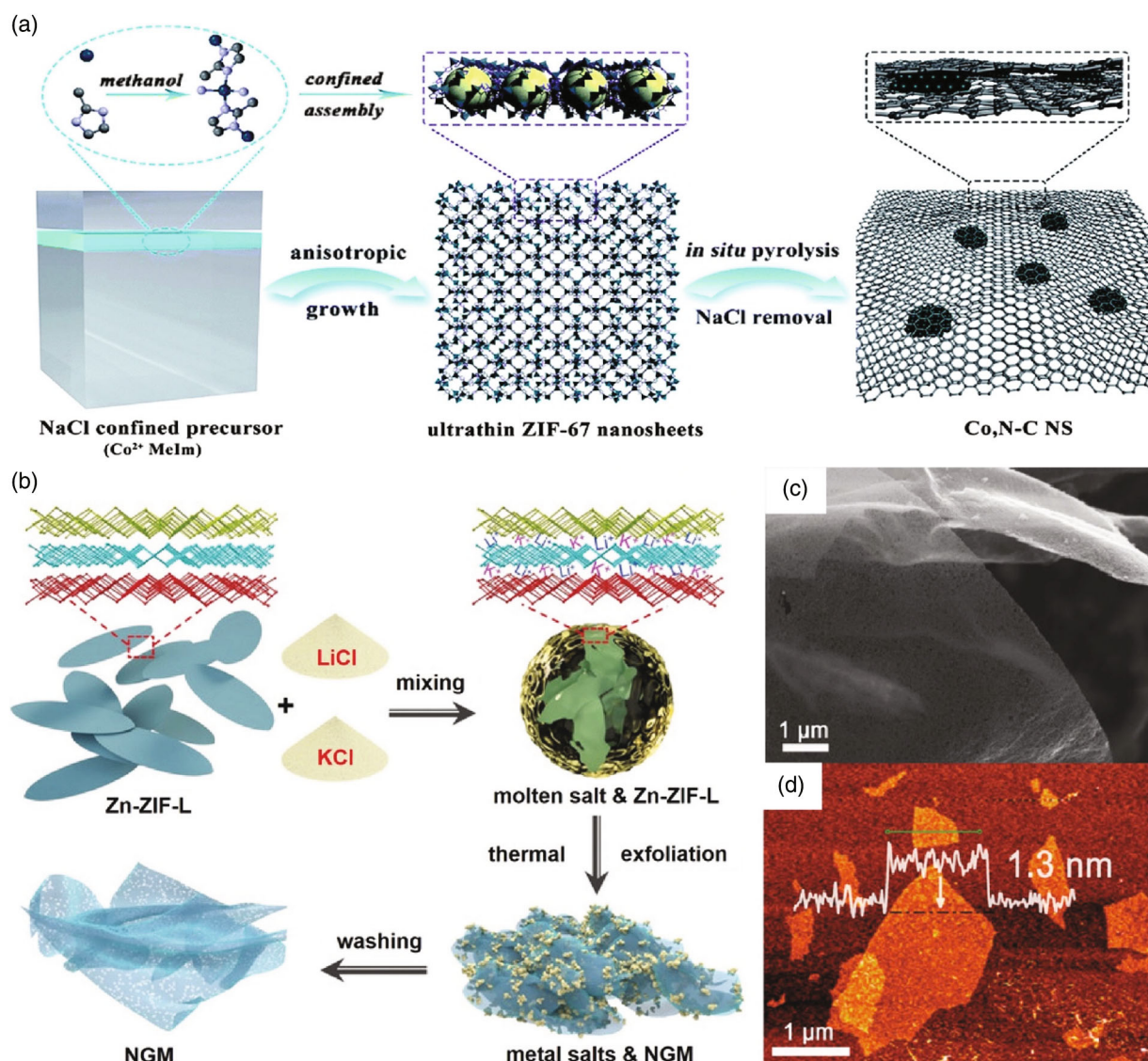
www.advenergysustres.com

Figure 13. a) Schematic of the synthesis procedure of ZIF-67 NSs and Co,N-CNS via salt template-confined in situ growth and calcination strategies. Reproduced with permission.[99] Copyright 2017, Royal Society of Chemistry. b) Schematic illustration of NGM synthesized by Zn-ZIF-L thermal exfoliation; c) SEM image of NGM-800; d) AFM image of NGM-800. (b–d) Reproduced with permission.[100] Copyright 2019, Wiley-VCH Verlag GmbH & Co. KGaA.

To realize the periodic layered structure, 2MeIm ligands as the key connections between the sodalite layers have to be interrupted by water. Instead of forming the coordination bond with the transition metal center, the existence of hydrogen bonds between H_2O molecules and N—H···N in 2MeIm is noted. These hydrogen bonds further facilitate the N—H···N hydrogen bonds with other 2MeIm. The interconnection of sodalite layers forms ZIF nanoleaves.[106,107] AFM showed that the $Co_{0.6}Zn_{0.4}$-ZIF nanoleaves had a thickness of 160 nm. Through a different temperature from 700 to 900 K, the $Co_{0.6}Zn_{0.4}$-ZIF nanoleaves can undergo pyrolysis to achieve a 2D leaf-like $Co_{0.6}$-N/C-T under N_2 atmosphere. Subsequently, by acid etching, the left Co species produced, and the Zn species were carefully removed after pyrolysis. Furthermore, the metal Co in Co-ZIF and bimetallic Co_xZn_{1-x}-ZIF play completely distinct roles during the

carbonization process. During carbonization, some micropores become mesopores due to the formation of Co NPs, which further aggregate and damage the pore structure. Such mesopores are formed when the Co NPs have been completely removed from the structure by acid treatment. Therefore, the current experiments have fully confirmed the coexistence of micropores and mesopores in Co_xZn_{1-x}-ZIF and Co-ZIF-derived carbons.[108] The XPS results confirmed the presence of $Co–N_x$, which has been identified as an active site for ORR.[109a] $Co_{0.6}$-N/C-800 exhibited a positive $E_{onset} = 0.916$ V and $E_{1/2} = 0.825$ V, showing a comparable performance with that of 20 wt% Pt/C ($E_{onset} = 0.926$ V and $E_{1/2} = 0.811$ V).

Benzimidazole (HBIM) was selected as the organic ligand to fabricate the ultrasmall 2D bimetallic MOF NSs ($M_2(BIM)_4$ NSs) using a bottom-up strategy with the assistance of triethylamine–

**ADVANCED
SCIENCE NEWS**

www.advancedsciencenews.com

**ADVANCED
ENERGY & SUSTAINABILITY
RESEARCH**
Open Access

www.advenergysustres.com

polyvinylpyrrolidone (TEA–PVP).[110] The $Co_xZn_{2−x}$–TEA complex solution was first obtained by mixing the metal ions (1.25x mmol of Co^{2+} and 1.25(2−x) mmol Zn^{2+}) and triethylamine (TEA) with polyvinylpyrrolidone (PVP) as the stabilizer. Then, the mixed solution containing TEA and HBIM was added to the $Co_xZn_{2−x}$-TEA complex solution to obtain $Co_xZn_{2−x}(BIM)_4$ NSs by ultrasonication. For comparison, the bulk M_2BIM_4 was synthesized in the absence of TEA and PVP. The XRD showed the increased interlayer distance along the [001] direction of the M_2BIM_4 NSs than that of the bulk M_2BIM_4. The larger interlayer distance can be attributed to the small molecules attached to the adjacent layers (e.g., TEA and solvents), which prevent the agglomeration of adjacent layers induced by the weak van der Waals forces[111] and the promotion of the ultrathin 2D M_2BIM_4 NS formation. The AFM showed that the thickness of individual $Co_{0.8}Zn_{1.2}(BIM)_4$ NSs was about 2 nm. Subsequently, the Co nanodots covered by the few-layer graphene (Co@FLG-40) were prepared through carbonization of the as-prepared $Co_xZn_{2−x}(BIM)_4$ NSs. The Co@FLG-40 displayed $E_{1/2}$ of 0.824 V and j_d of 6.42 mA cm$^{−2}$ for the four-electron ORR pathway. The experimental studies and DFT calculations showed that great O_2 absorptivity realized by the abundant Co–N_x, and pyridinic-N in the few-layer graphene shell determines the remarkable ORR electrocatalysis of Co@FLG. Meanwhile, the excellent electron-depletion ability of Co to the few-layer graphene shell elevates the e_g orbital energy of Co(II) to dissociate the O=O/O—O bonds. Moreover, the well-wrapped Co nanodots maximize the electron overflow capability of Co nanodots to enhance the activity of Co–N_x and pyridinic-N for the O=O/O—O cleavages. The facile dissociation of the O=O/O—O bonds strongly decreases the Gibbs free energy (ΔG) change of the ORR.[112]

3.2. Phthalocyanine- and Porphyrin-Based Ligands

Transition metal macrocyclic compounds based on phthalocyanine and porphyrin were first discovered to have the catalytic capacity of ORR in 1964, but the activity and stability of such catalysts are relatively low.[113] The study of such macrocyclic catalysts is based on the M–N4 coordination structure, the preparation of derivatives can further regulate the electronic structure to improve the ORR performance. However, these macrocyclic compounds are expensive, where the structures are easily broken after high heat treatment. In recent years, various coordination elements have been derived from phthalocyanine and porphyrin rings to coordinate transition metals for more active sites.[16b,114]

Based on the solvothermal method, the synthesized building blocks 2,3,9,10,16,17,23,24-octahydroxyphthalocyaninato copper (PcCu-(OH)_8) construct a copper phthalocyanine-based 2D-conjugated MOF, in which the cobalt bis(dihydroxy) complex (Co–O_4) is the connection site (PcCu–O_8–Co) (**Figure 14**a,b).[114] The optimized spin state of the cobalt node shows the unpaired electron in the σ^* antibonding orbital ($e_g = 1$), which activates the high ORR electroactivity of Co–O_4 centers.[115] The as-prepared PcCu–O_8–Co hybridized with carbon nanotubes (PcCu–O_8–Co/CNTs) demonstrates a high ORR activity in the alkaline environment ($E_{1/2} = 0.83$ V vs RHE, $n = 3.39$, $j_d = 5.3$ mA cm$^{−2}$).

The HRTEM and the corresponding selected-area electron diffraction (SAED) image revealed the repeated unit of PcCu–O_8–Co architecture, and each unit size is around 1.75 nm. In terms of the pore-size distribution, PcCu–O_8–Co has significant micropores with a size of 1.5 nm and mesopores with sizes ranging from 2 to 10 nm, both promoting the oxygen and electrolyte conduction. The DFT calculations investigated the structure of the single-layer 2D MOF with different stacking types of PcCu–O_8–Co, in which the AA-serrated stacking type is most energetically preferred. Compared with Cu–N, DFT calculations showed that the linking Co sites as the active sites prefer the adsorption of intermediate OOH$^−$ (Figure 14c).[82,116] In addition, the combination of the Raman spectro–electrochemistry and the theoretical calculation confirmed that the Co–O centers in PcCu–O_8–Co were the catalytic active site of ORR. Raman spectra revealed a new peak of 691 cm$^{−1}$ during the ORR. The increased intensity of the peak with the increased overpotential demonstrated that more oxygen-related species are accumulated under larger overpotential (Figure 14d,e). Based on the derived data, a possible ORR mechanism was proposed (Figure 14f).

Recently, 2D porphyrin-based covalent organic polymers (COPs) were prepared using porphyrin as the monomer.[16b] After further carbonization, they supported good electrocatalytic activities toward the ORR process. For example, by the Friedel–Crafts catalysts, COP-TPP was prepared based on Scholl reaction to remove the two aryl-bound hydrogen atoms of meso-tetraphenyl-porphyrin. COP polymerization occurs within its confined space with MOF-180 as the template. The COP materials (COP-TPP@MOF) were prepared by removing the template via HCl treatment (Figure 14g). Then, the further incorporation of metal ions to the as-synthesized COP-TPP@MOF forms COP-TPP(M)@MOF, where M = Fe, and/or Co, and this is further followed by carbonization (COP-TPP(M)@MOF-T °C) to improve the electroactivity to the ORR. The Fe/Co codoped COP-derived carbon shows better ORR performance than the single Co-doped COP-derived carbon (Figure 14h). The 2D charge density distribution revealed that Fe or Co doping leads to the increasing of positive charge density at the metal–N_x coordination sites (Figure 14i,j). The 3D charge density distribution showed that the positive charge density was located at metal–N_x coordination sites whereas the negative charge density was anchored at carbon atoms (Figure 14k). In addition, theoretical calculations confirmed that the initial adsorption of O_2 was the RDS of the ORR process for Fe/Co-doped COP-TPP. Meanwhile, the COP-TPP shows the final desorption as the RDS (Figure 14l).

The exfoliated 2D laminar CAN-Pc(M) (M = Fe, Co, and Fe/Co) was synthesized by the ball-milling method of polyphthalocyanine, followed by dispersion in N_2-saturated ethanol. The Fe–N_4 and Co–N_4 sites appeared in one connected plane with four aromatic rings as electroactive sites for the ORR.[9b] The best catalytic activity of the ORR is realized in CAN-Pc(Fe/Co) with an atomic ratio of Fe/Co = 25:75. The delamination of polyphthalocyanine and the formation of 2D laminar CAN-Pc(M)PXRD have been proved by the PXRD pattern after mechanical shearing. The lamellar features of the material have been observed by AFM images and the corresponding height profiles of CAN-Pc(M). The metal density of CAN-Pc(Fe/Co) was similar to the theoretical calculated metal density of single-layered CAN-Pc(Fe/Co). Furthermore, the CAN-Pc(Fe/Co) electrode exhibited most
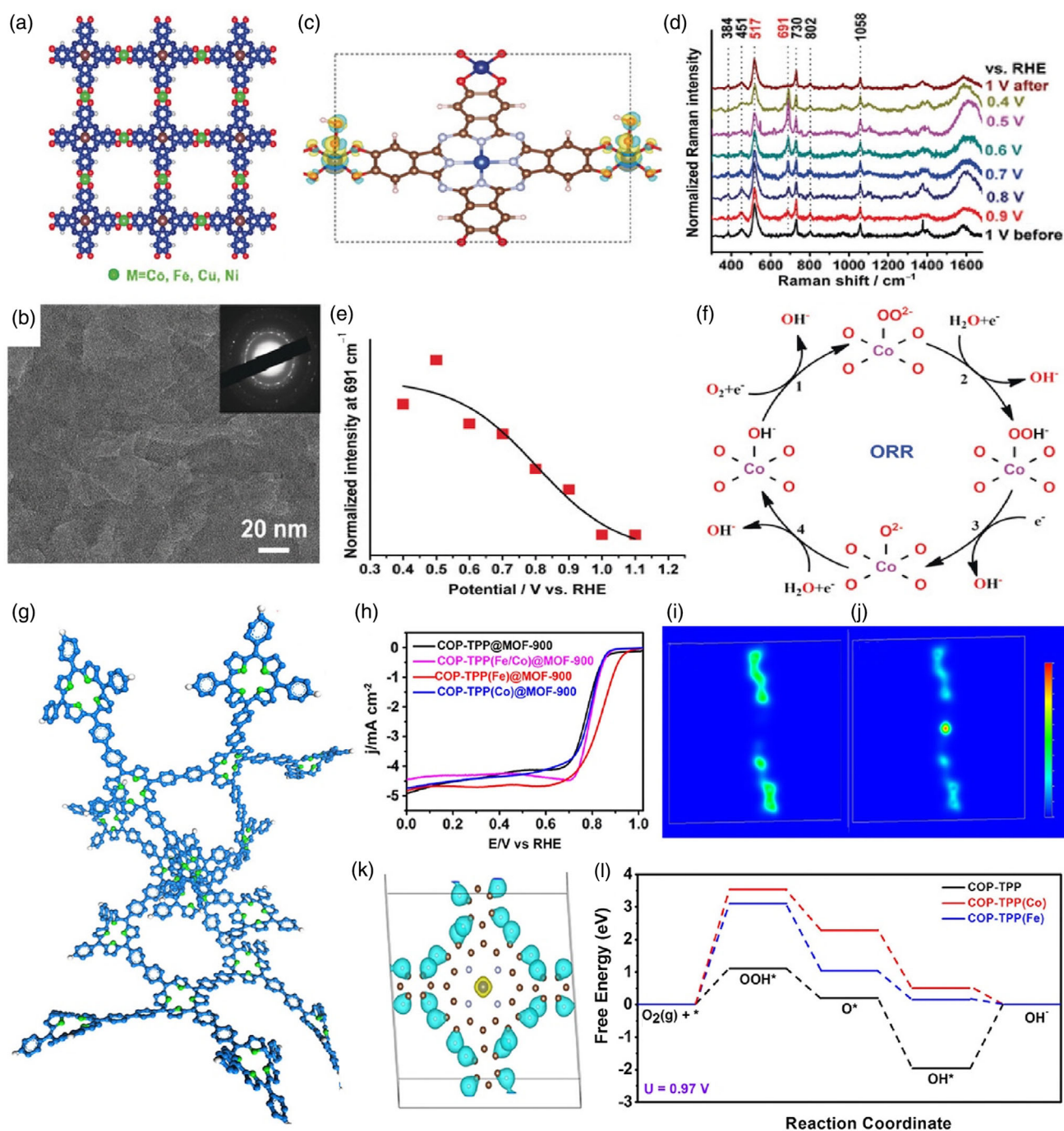
Figure 14. a) Schematic structure of PcCu–O$_8$–Co–M (M = Co, Fe, Cu, Ni); b) TEM image of PcCu–O$_8$–Co; c) the differential charge density image of PcCu–O$_8$–Co with OOH$^-$ intermediates on the Co–O sites; d,e) in situ Raman analysis during the ORR process; f) proposed reaction mechanism. (a–f) Reproduced with permission.[114] Copyright 2019, Wiley-VCH Verlag GmbH & Co. KGaA. g) Structure of COP-TPP@MOF catalyst. h) Polarization curves of COP-TPP(M)@MOF-900 (M = Fe and/or Co). The 2D charge density distribution images of i) COP-TPP@MOF and j) COP-TPP(M)@MOF. k) The 3D charge density distribution image of COP-TPP(M)@MOF. l) The schematic energy profiles for the ORR process on COP-TPP(M)@MOF catalysts in alkaline conditions. g–l) Reproduced with permission.[16b] Copyright 2017, American Chemical Society.

positive $E_{onset} = 1.04$ V and $E_{1/2} = 0.84$ V, along with a large cathodic diffusion current density of 5.23 mA cm^{-2}, which was better than the benchmark of the Pt/C electrode ($E_{onset} = 1.02$ V and $E_{1/2} = 0.84$ V at a loading mass of 100 µg cm^{-2}). Meanwhile, CAN-Pc(Fe/Co) also displayed a smaller Tafel slope to support their high reaction kinetics.

ADVANCED
SCIENCE NEWS
www.advancedsciencenews.com

ADVANCED
ENERGY & SUSTAINABILITY
RESEARCH
Open Access
www.advenergysustres.com

3.3. Carboxylic Acid Donor Ligands

The activity of ORR is low in the synthesis of 2D MOFs nanomaterials with a single binary carboxylic acid ligand (e.g., BDC). The performance of ORR can be improved by double-ligand coordination with the nitrogen-containing ligand and embedded low content of platinum NPs in ultrathin 2D MOF NSs.[64,102] For instance, 2D Co-based MOFs were synthesized by 5-hydroxyisophthalic acid (HO-BDC) and 2,2′-(oxybis(methylene))bis (1H-benzo[d]imidazole) (Hbbop) ligands.[117] The N-doped carbon matrix (Co_3O_4@N/C) was prepared by 2D Co-MOF as the precursor and graphitic carbon nitride (g-C_3N_4) as the nitrogen source. The Co_3O_4@N/C showed excellent ORR performance due to the well-dispersed Co_3O_4 and N-doped active species and synergetic chemical coupling effects among components. Also, 2D Co-MOFs [Co(BDC)$_2$(SPDP)$_2$(DMF)(H$_2$O)] (SPDP = 4,4′-(sulfonylbis (4,1-phenylene))dipyridine) can be used to wrap the Co_9S_8 nanocomposites to supply a carbon shell with N, O, and S doping.[64] The excellent catalytic activity originated from the unique advantages of the synthesized structures.

In addition, a multishell 2d MOFs were prepared and transferred to a Co/Ni-embedded bimetallic N-doped porous carbon.[96a] The NiCo dual-metal MOF NSs were synthesized using Co^{2+} and Ni^{2+} as metal centers. The additional 2MeIm adsorbs Co^{2+} on the NiCo MOF surface, which further induces the assembly of 2D NiCo MOFs. Co/Ni-contained N-doped porous carbons (NiCo-NC) were obtained after the pyrolysis in N_2 at 900 °C. The thickness of NSs was less than 15 nm. Based on the Pearson acid–base concept, both Ni^{2+} and Co^{2+} are the borderline acids. Meanwhile, carboxylate is a hard base and imidazole acts as the borderline base.[20a] Due to the weak interaction trend between the hard base and borderline acids, the linker exchanging was initiated by adding 2MeIm. The NiCo-NC showed high activities ($E_{1/2} = 0.866$ V vs RHE, $n = 3.90$, $E_{onset} = 1.038$ V), similar to the commercial Pt/C.

Recently, novel composite nanomaterial ultrathin 2D MOF NSs have been synthesized by embedding the Pt NPs.[102] Due to the synergistic effects between Pt NPs and MOFs, the electroactivities of the composite of OER on MOFs and ORR on Pt NPs have been optimized through the electronic modulation between Pt and metal node sites. 2D MOF NSs (NiNSMOFs) and Pt@NSMOFs were prepared under constant ultrasonication conditions (BDC as the organic ligand) (**Figure 15**a,b). The TEM image showed that the Pt@NSMOFs sample embedded with Pt NPs maintained a shape similar to NiNSMOFs (Figure 15c). The ultrathin structure of the MOF samples was confirmed by AFM (Figure 15d). The thickness of NiNSMOFs and Pt@NiNSMOFs is determined to be 1.9 and 3.7 nm, respectively. When the Pt loading increased from 0.7% to 3.2%, a positive onset potential shifts from 0.902 to 1.024 V, corresponding to the enhanced ORR activity. However, as Pt loading further increases to 8.8 wt%, the ORR performance becomes worse. To understand the energetic trend of the ORR process, theoretical calculations apply a Pt (111) surface absorbed with a single-metal node connected with a ligand molecule to analyze the free energy changes. The introduced metal–organic groups on the Pt surface largely alleviate the energy barrier of the ORR process, thus increasing the catalytic activity of the modified Pt surface (Figure 15e–g).

4. Conclusions and Perspectives

In summary, we have highlighted recent advances in the preparation of 2D MOF NSs with different organic ligands and different methods for electrocatalytic OER and ORR. The organic ligands largely determine the electrocatalytic performance. Different ligands have different advantages. The organic ligands used in OER are mainly expanded by BDC, whereas the imidazole ring dominates the ORR. Sonication synthesis was the most widely used bottom-up method, and a variety of 2D MOF NSs have been successfully synthesized in suitable solvents.[11c,12b,20a,31] In addition, some other 2D MOF synthesis methods have been successfully introduced, such as modulated synthesis, interfacial synthesis, three-layer synthesis, and surfactant-assisted synthesis.

Although advanced progress has been achieved in 2D MOFs-based electrocatalysts for realizing efficient water splitting, future development is perhaps still in the infancy, which faces many challenges for further investigations. Currently, the high price of organic ligands and the harsh synthesis requirements are still limiting the developments of the large-scale synthesis of 2D MOFs. Meanwhile, the limited synthesis methods with poor controllability of the thickness are other important challenges that have to be addressed in future research.

The ideal electrocatalyst usually displays several important features including high intrinsic catalytic activity, abundant exposed active sites, superior electron and mass transfer efficiency, as well as long-term stability.[118] The modification of various functional groups (e.g., –Br, –OCH$_3$, –F, –OH, and –NH$_2$) and organic ligands is also an essential factor that must be considered in the rational design of an ideal 2D MOF electrocatalyst. The introduction of these functional groups not only stimulates defect strain but also tailors the binding energies of the surface-mounted MOFs for enhanced catalytic activity.[45,46a,c,d,e,g,52a] Moreover, due to superior electroactivity and stability, the combination of 2D MOF composites with many inorganic functional materials has been intensively studied, some of which have demonstrated a highly efficient electroactivity toward water splitting.

As we look to the future, 2D MOFs and their derived materials show great potential in many electrochemical applications such as electrochemical sensors, water splitting, and lithium-ion batteries. As OER and ORR electrocatalysts, there are still some obstacles to be overcome and space for further performance improvement. The following strategies can be considered to improve the OER and ORR activity of 2D MOFs-based electrocatalysts. 1) Most kinds of MOFs are nonconductive. The conductive organic ligands with conjugated bonds were selected to build conductive 2D MOFs to improve the conductivity of the electrocatalysts.[119] 2) The defect-related strain effect in MOFs was introduced by various functional groups (such as electron-absorbing group and electron-donating group) to enhance the catalytic activity. 3) The nonmetal doping strategy can further increase the catalytic activity and stability. Especially as ORR electrocatalysts, 2D MOFs are rarely used directly as ORR electrocatalysts. Most of them are pyrolytic organic compounds rich in N atoms. 4) Most organic ligands are expensive, and different ligands have different advantages. The two and more simple organic ligands with different advantages to coordinate with
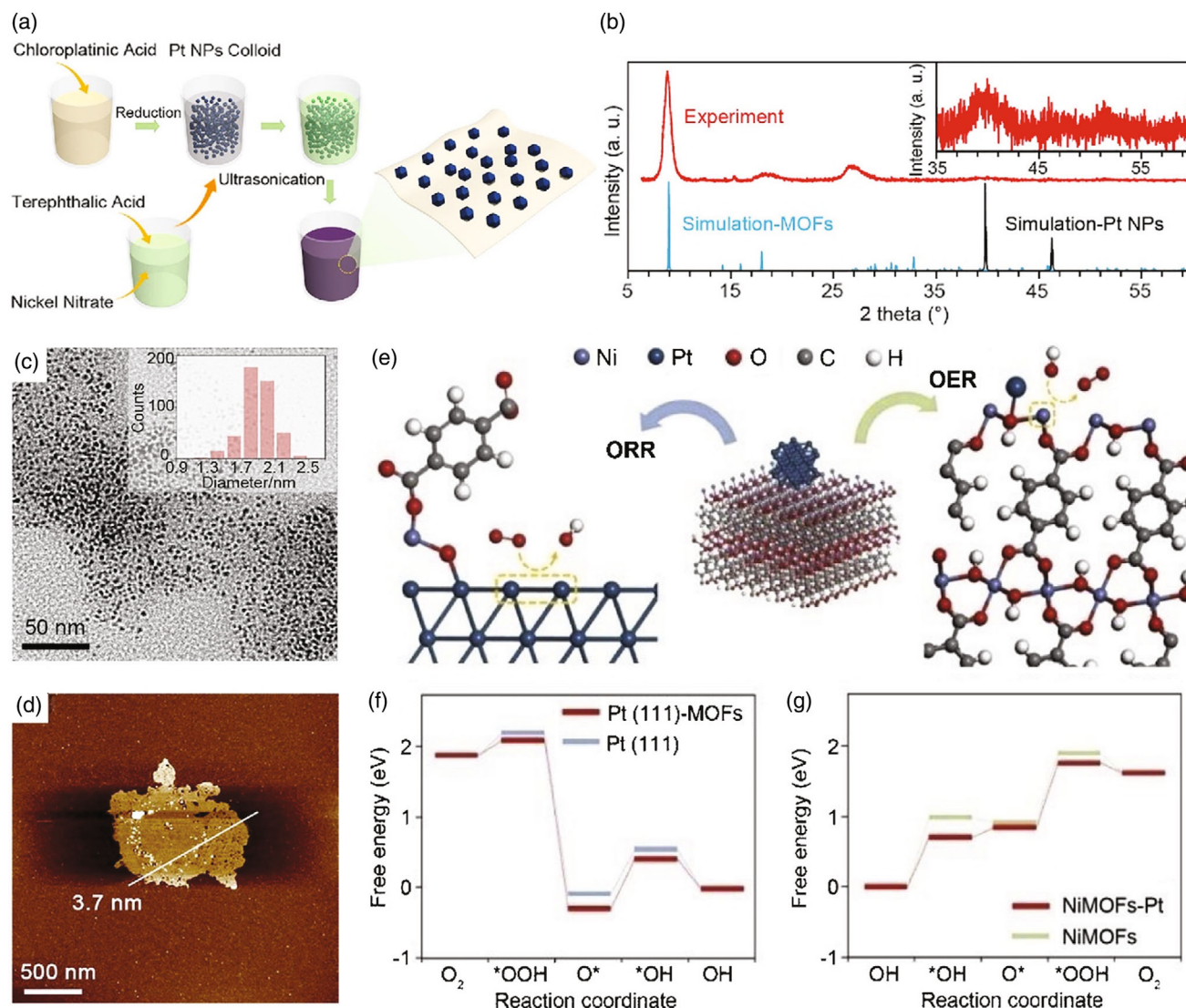
Figure 15. a) Schematic of the synthetic process for Pt@NSMOFs; b) experimental and simulation XRD patterns of Pt@NiNSMOFs (the enlarged pattern is shown in the inset); c) TEM image of Pt@NiNSMOFs; d) AFM image of Pt@NiNSMOFs; e) schematic of the model of Pt-embedded MOFs for DFT calculations; free energy diagrams for f) ORR and g) OER pathways in alkaline conditions. (a–g) Reproduced with permission.[102] Copyright 2019, Elsevier B.V.

metal ions can be selected to achieve a complementary effect. Compared with traditional porous materials, 2D MOF composites have the advantages of the simple fabrication process, large specific surface area, and controllable size, which will continuously inspire more research in electrocatalyst fields.

The MOF-derivative materials are also becoming the most promising candidates in electrocatalysis, including porous carbon, doped carbon materials, metal-based materials, and even metal oxides. These materials usually indicate abundant advantages such as the simple synthesis, the well-preserved large specific surface area, and porosity from the MOF framework.[120] Moreover, the high controllability in dopants, morphologies, and compositions endows MOF-derivate materials great potential in future broad applications beyond ORR and OER.[121]

Among these materials, the highly conductive porous carbon satisfies the proposed strategy for ORR/OER electrocatalysts, which shows fast charge transfer/mass transport as well as the maximum exposure of active sites.[122] Moreover, porous carbon can also function as efficient support to load other electroactive material. The metals at the nodes of MOF enable the flexible transformation into the atomic catalyst, metal oxides, transition metal-based LDHs, and even alloys with unique structures and morphologies. These materials not only possess abundant electroactive sites or regions but also optimize the electronic structures to achieve efficient electron transfer and appropriate binding strength. Therefore, investigating the MOF derivative supplies another advanced avenue for developing novel electrocatalysts in ORR and OER.

Acknowledgements

Conflict of Interest

The authors declare no conflict of interest.

Keywords

[1] C. Tan, X. Cao, X.-J. Wu, Q. He, J. Yang, X. Zhang, J. Chen, W. Zhao, S. Han, G.-H. Nam, M. Sindoro, H. Zhang, *Chem. Rev.* **2017**, *117*, 6225.

[2] a) M. Xu, T. Liang, M. Shi, H. Chen, *Chem. Rev.* **2013**, *113*, 3766; b) S.-T. Hsiao, C.-C. M. Ma, H.-W. Tien, W.-H. Liao, Y.-S. Wang, S.-M. Li, Y.-C. Huang, *Carbon* **2013**, *60*, 57.

[3] G. Li, Y. Li, H. Liu, Y. Guo, Y. Li, D. Zhu, *Chem. Commun.* **2010**, *46*, 3256.

[4] Y. Zhao, L. Zhang, W. Wei, Y. Li, A. Liu, Y. Zhang, S. Liu, *RSC Adv.* **2015**, *5*, 82879.

[5] a) M. Chhowalla, H. S. Shin, G. Eda, L.-J. Li, K. P. Loh, H. Zhang, *Nat. Chem.* **2013**, *5*, 263; b) S.-L. Li, K. Tsukagoshi, E. Orgiu, P. Samori, *Chem. Soc. Rev.* **2016**, *45*, 118.

[6] a) P. Niu, L. Zhang, G. Liu, H.-M. Cheng, *Adv. Funct. Mater.* **2012**, *22*, 4763; b) S. Yang, Y. Gong, J. Zhang, L. Zhan, L. Ma, Z. Fang, R. Vajtai, X. Wang, P. M. Ajayan, *Adv. Mater.* **2013**, *25*, 2452.

[7] a) R. Ma, T. Sasaki, *Adv. Mater.* **2010**, *22*, 5082; b) L. Wang, T. Sasaki, *Chem. Rev.* **2014**, *114*, 9455.

[8] a) D. Golberg, Y. Bando, Y. Huang, T. Terao, M. Mitome, C. Tang, C. Zhi, *ACS Nano* **2010**, *4*, 2979; b) Y. Lin, T. V. Williams, J. W. Connell, *J. Phys. Chem. Lett.* **2010**, *1*, 277.

[9] a) Z. Zhang, Y. Qin, M. Dou, J. Ji, F. Wang, *Nano Energy* **2016**, *30*, 426; b) S. Yang, Y. Yu, M. Dou, Z. Zhang, L. Dai, F. Wang, *Angew. Chem., Int. Ed.* **2019**, *58*, 14724.

[10] a) S. Mohnani, D. Bonifazi, *Coord. Chem. Rev.* **2010**, *254*, 2342; b) Y. Zhao, J. Ling, S. Li, M. Li, A. Liu, S. Liu, *J. Mater. Chem. A* **2018**, *6*, 2828.

[11] a) Y. Huang, M. Zhao, S. Han, Z. Lai, J. Yang, C. Tan, Q. Ma, Q. Lu, J. Chen, X. Zhang, Z. Zhang, B. Li, B. Chen, Y. Zong, H. Zhang, *Adv. Mater.* **2017**, *29*, 1700102; b) B. Han, X. Ou, Z. Deng, Y. Song, C. Tian, H. Deng, Y.-J. Xu, Z. Lin, *Angew. Chem., Int. Ed.* **2018**, *57*, 16811; c) A. Dhakshinamoorth, A. M. Asiri, H. Garcia, *Adv. Mater.* **2019**, *31*, 1900617; d) R. Sakamoto, K. Takada, X. Sun, T. Pal, T. Tsukamoto, E. J. H. Phua, A. Rapakousiou, K. Hoshiko, H. Nishihara, *Coord. Chem. Rev.* **2016**, *320*, 118.

[12] a) S. Bhattacharyya, C. Das, T. K. Maji, *RSC Adv.* **2018**, *8*, 26728; b) M. Zhao, Y. Huang, Y. Peng, Z. Huang, Q. Ma, H. Zhang, *Chem. Soc. Rev.* **2018**, *47*, 6267.

[13] S. Jin, *ACS Energy Lett.* **2019**, *4*, 1443.

[14] a) X. Liu, Z. Chang, L. Luo, T. Xu, X. Lei, J. Liu, X. Sun, *Chem. Mater.* **2014**, *26*, 1889; b) Z. Kou, B. Guo, D. He, J. Zhang, S. Mu, *ACS Energy Lett.* **2018**, *3*, 184.

[15] a) T. Zhan, Y. Zhang, X. Liu, S. Lu, W. Hou, *J. Power Sources* **2016**, *333*, 53; b) Z. Li, H. Sun, L. Wei, W.-J. Jiang, M. Wu, J.-S. Hu, *ACS Appl. Mater. Interfaces* **2017**, *9*, 5272.

[16] a) D. Ansovini, C. J. J. Lee, C. S. Chua, L. T. Ong, H. R. Tan, W. R. Webb, R. Raja, Y.-F. Lim, *J. Mater. Chem. A* **2016**, *4*, 9744; b) J. Guo, Y. Li, Y. Cheng, L. Dai, Z. Xiang, *ACS Nano* **2017**, *11*, 8379; c) D. Khang Ngoc, P. Zheng, Z. Dai, Y. Zhang, R. Dangol, Y. Zheng, B. Li, Y. Zong, Q. Yan, *Small* **2018**, *14*, 1703257.

[17] Z. Jiang, Z.-J. Jiang, T. Maiyalagan, A. Manthiram, *J. Mater. Chem. A* **2016**, *4*, 5877.

[18] a) K. Xiang, J. Guo, J. Xu, T. Qu, Y. Zhang, S. Chen, P. Hao, M. Li, M. Xie, X. Guo, W. Ding, *ACS Appl. Energy Mater.* **2018**, *1*, 4040; b) Y. Zhang, T. Qu, F. Bi, P. Hao, M. Li, S. Chen, X. Guo, M. Xie, X. Guo, *ACS Sustainable Chem. Eng.* **2018**, *6*, 16859; c) S. Chen, F. Bi, K. Xiang, Y. Zhang, P. Hao, M. Li, B. Zhao, X. Guo, *ACS Sustainable Chem. Eng.* **2019**, *7*, 15278.

[19] M. Zhao, Q. Lu, Q. Ma, H. Zhang, *Small Methods* **2017**, *1*, 1600030.

[20] a) S. Zhao, Y. Wang, J. Dong, C.-T. He, H. Yin, P. An, K. Zhao, X. Zhang, C. Gao, L. Zhang, J. Lv, J. Wang, J. Zhang, A. M. Khattak, N. A. Khan, Z. Wei, J. Zhang, S. Liu, H. Zhao, Z. Tang, *Nat. Energy* **2016**, *1*, 16184; b) G. Hai, X. Jia, K. Zhang, X. Liu, Z. Wu, G. Wang, *Nano Energy* **2018**, *44*, 345; c) J. Xie, X. Zhang, H. Zhang, J. Zhang, S. Li, R. Wang, B. Pan, Y. Xie, *Adv. Mater.* **2017**, *29*, 1604765.

[21] a) C. L. Xiao, Y. B. Li, X. Y. Lu, C. Zhao, *Adv. Funct. Mater.* **2016**, *26*, 3515; b) S. Mukhopadhyay, J. Debgupta, C. Singh, A. Kar, S. K. Das, *Angew. Chem., Int. Ed.* **2018**, *57*, 1918; c) J. Q. Shen, P. Q. Liao, D. D. Zhou, C. T. He, J. X. Wu, W. X. Zhang, J. P. Zhang, X. M. Chen, *J. Am. Chem. Soc.* **2017**, *139*, 1778; d) F. L. Li, Q. Shao, X. Q. Huang, J. P. Lang, *Angew. Chem., Int. Ed.* **2018**, *57*, 1888; e) F. Z. Sun, G. Wang, Y. Q. Ding, C. Wang, B. B. Yuan, Y. Q. Lin, *Adv. Energy Mater.* **2018**, *8*, 1800584.

[22] Q. Yin, J. M. Tan, C. Besson, Y. V. Geletii, D. G. Musaev, A. E. Kuznetsov, Z. Luo, K. I. Hardcastle, C. L. Hill, *Science* **2010**, *328*, 342.

[23] J. Duan, S. Chen, C. Zhao, *Nat. Commun.* **2017**, *8*, 15341.

[24] a) H.-C. Zhou, J. R. Long, O. M. Yaghi, *Chem. Rev.* **2012**, *112*, 673; b) H.-C. J. Zhou, S. Kitagawa, *Chem. Soc. Rev.* **2014**, *43*, 5415; c) H. Furukawa, K. E. Cordova, M. O'Keeffe, O. M. Yaghi, *Science* **2013**, *341*, 1230444.

[25] J. He, M. Zeller, A. D. Hunter, Z. Xu, *J. Am. Chem. Soc.* **2012**, *134*, 1553.

[26] Y. Wang, M. Zhao, J. Ping, B. Chen, X. Cao, Y. Huang, C. Tan, Q. Ma, S. Wu, Y. Yu, Q. Lu, J. Chen, W. Zhao, Y. Ying, H. Zhang, *Adv. Mater.* **2016**, *28*, 4149.

[27] K. Fan, H. Chen, Y. Ji, H. Huang, P. M. Claesson, Q. Daniel, B. Philippe, H. Rensmo, F. Li, Y. Luo, L. Sun, *Nat. Commun.* **2016**, *7*, 11981.

[28] M. Bajdich, M. Garcia-Mota, A. Vojvodic, J. K. Norskov, A. T. Bell, *J. Am. Chem. Soc.* **2013**, *135*, 13521.

[29] a) N. Li, D. K. Bediako, R. G. Hadt, D. Hayes, T. J. Kempa, F. von Cube, D. C. Bell, L. X. Chen, D. G. Nocera, *Natl. Acad. Sci. USA* **2017**, *114*, 1486; b) M. S. Burke, M. G. Kast, L. Trotochaud, A. M. Smith, S. W. Boettcher, *J. Am. Chem. Soc.* **2015**, *137*, 3638; c) M. Goerlin, P. Chernev, J. F. de Araujo, T. Reier, S. Dresp, B. Paul, R. Kraehnert, H. Dau, P. Strasser, *J. Am. Chem. Soc.* **2016**, *138*, 5603.

[30] a) L. C. Seitz, C. F. Dickens, K. Nishio, Y. Hikita, J. Montoya, A. Doyle, C. Kirk, A. Vojvodic, H. Y. Hwang, J. K. Norskov, T. F. Jaramillo, *Science* **2016**, *353*, 1011; b) J. Mahmood, F. Li, S.-M. Jung,

M. S. Okyay, I. Ahmad, S.-J. Kim, N. Park, H. Y. Jeong, J.-B. Baek, *Nat. Nanotechnol.* **2017**, *12*, 441.

[31] C. Guo, Y. Jiao, Y. Zheng, J. Luo, K. Davey, S.-Z. Qiao, *Chem* **2019**, *5*, 2429.

[32] D. Zhu, J. Liu, L. Wang, Y. Du, Y. Zheng, K. Davey, S.-Z. Qiao, *Nanoscale* **2019**, *11*, 3599.

[33] X. Wei, N. Li, N. Liu, *Electrochim. Acta* **2019**, *318*, 957.

[34] K. Rui, G. Zhao, Y. Chen, Y. Lin, Q. Zhou, J. Chen, J. Zhu, W. Sun, W. Huang, S. X. Dou, *Adv. Funct. Mater.* **2018**, *28*, 1801554.

[35] X. Wang, J. Zhuang, Q. Peng, Y. D. Li, *Nature* **2005**, *437*, 121.

[36] F.-L. Li, P. Wang, X. Huang, D. J. Young, H.-F. Wang, P. Braunstein, J.-P. Lang, *Angew. Chem., Int. Ed.* **2019**, *58*, 7051.

[37] Q. Hu, X. Huang, Z. Wang, G. Li, Z. Han, H. Yang, X. Ren, Q. Zhang, J. Liu, C. He, *J. Mater. Chem. A* **2020**, *8*, 2140.

[38] a) G. A. Tompsett, W. C. Conner, K. S. Yngvesson, *Chemphyschem* **2006**, *7*, 296; b) L. Lv, Z. Yang, K. Chen, C. Wang, Y. Xiong, *Adv. Energy Mater.* **2019**, *9*, 1803358.

[39] J. Li, D. Wu, J. Iocozzia, H. Du, X. Liu, Y. Yuan, W. Zhou, Z. Li, Z. Xue, Z. Lin, *Angew. Chem., Int. Ed.* **2019**, *58*, 1985.

[40] J. Zhou, Y. Dou, A. Zhou, L. Shu, Y. Chen, J.-R. Li, *ACS Energy Lett.* **2018**, *3*, 1655.

[41] J. Xu, X. Zhu, X. Jia, *ACS Sustainable Chem. Eng.* **2019**, *7*, 16629.

[42] Y. Xu, B. Li, S. Zheng, P. Wu, J. Zhan, H. Xue, Q. Xu, H. Pang, *J. Mater. Chem. A* **2018**, *6*, 22070.

[43] B. Spingler, S. Schnidrig, T. Todorova, F. Wild, *Crystengcomm* **2012**, *14*, 751.

[44] L. Zhao, B. Dong, S. Li, L. Zhou, L. Lai, Z. Wang, S. Zhao, M. Han, K. Gao, M. Lu, X. Xie, B. Chen, Z. Liu, X. Wang, H. Zhang, H. Li, J. Liu, H. Zhang, X. Huang, W. Huang, *ACS Nano* **2017**, *11*, 5800.

[45] a) Z. Qiu, C.-W. Tai, G. A. Niklasson, T. Edvinsson, *Energy Environ. Sci.* **2019**, *12*, 572; b) D. Friebel, M. W. Louie, M. Bajdich, K. E. Sanwald, Y. Cai, A. M. Wise, M. J. Cheng, D. Sokaras, T. C. Weng, R. Alonso-Mori, R. C. Davis, J. R. Bargar, J. K. Norskov, A. Nilsson, A. T. Bell, *J. Am. Chem. Soc.* **2015**, *137*, 1305; c) M. Gong, H. Dai, *Nano Res.* **2015**, *8*, 23; d) J. Y. C. Chen, L. Dang, H. Liang, W. Bi, J. B. Gerken, S. Jin, E. E. Alp, S. S. Stahl, *J. Am. Chem. Soc.* **2015**, *137*, 15090; e) J. R. Petrie, C. Mitra, H. Jeen, W. S. Choi, T. L. Meyer, F. A. Reboredo, J. W. Freeland, G. Eres, H. N. Lee, *Adv. Funct. Mater.* **2016**, *26*, 1564; f) L. Wang, K. A. Stoerzinger, L. Chang, X. Yin, Y. Li, C. S. Tang, E. Jia, M. E. Bowden, Z. Yang, A. Abdelsamie, L. You, R. Guo, J. Chen, A. Rusydi, J. Wang, S. A. Chambers, Y. Du, *ACS Appl. Mater. Interfaces* **2019**, *11*, 12941; g) D. S. Raja, H.-W. Lin, S.-Y. Lu, *Nano Energy* **2019**, *57*, 1.

[46] a) W. Li, S. Xue, S. Watzele, S. Hou, J. Fichtner, A. L. Semrau, L. Zhou, A. Welle, A. S. Bandarenka, R. A. Fischer, *Angew. Chem., Int. Ed.* **2020**, *59*, 5837; b) G. Tsoukleri, J. Parthenios, K. Papagelis, R. Jalil, A. C. Ferrari, A. K. Geim, K. S. Novoselov, C. Galiotis, *Small* **2009**, *5*, 2397; c) D. Zhou, S. Wang, Y. Jia, X. Xiong, H. Yang, S. Liu, J. Tang, J. Zhang, D. Liu, L. Zheng, Y. Kuang, X. Sun, B. Liu, *Angew. Chem., Int. Ed.* **2019**, *58*, 736.

[47] C. Yang, A. Grimaud, *Catalysts* **2017**, *7*, 149.

[48] L. Zhuang, L. Ge, H. Liu, Z. Jiang, Y. Jia, Z. Li, D. Yang, R. K. Hocking, M. Li, L. Zhang, X. Wang, X. Yao, Z. Zhu, *Angew. Chem., Int. Ed.* **2019**, *58*, 13565.

[49] L. Zhuang, L. Ge, Y. Yang, M. Li, Y. Jia, X. Yao, Z. Zhu, *Adv. Mater.* **2017**, *29*, 1606793.

[50] M. Witman, S. Ling, S. Anderson, L. Tong, K. C. Stylianou, B. Slater, B. Smit, M. Haranczyk, *Chem. Sci.* **2016**, *7*, 6263.

[51] S. K. Ghosh, J.-P. Zhang, S. Kitagawa, *Angew. Chem., Int. Ed.* **2007**, *46*, 7965.

[52] J. Huang, Y. Li, R.-K. Huang, C.-T. He, L. Gong, Q. Hu, L. Wang, Y.-T. Xu, X.-Y. Tian, S.-Y. Liu, Z.-M. Ye, F. Wang, D.-D. Zhou, W.-X. Zhang, J.-P. Zhang, *Angew. Chem., Int. Ed.* **2018**, *57*, 4632.

[53] A. D. Allen, M. Sumonja, T. T. Tidwell, *J. Am. Chem. Soc.* **1997**, *119*, 2371.

[54] W. Li, W. Fang, W. Chen, K. Dinh, H. Ren, L. Zhao, C. Liu, Q. Yan, *J. Mater. Chem. A* **2020**, *8*, 3658.

[55] J. Suntivich, K. J. May, H. A. Gasteiger, J. B. Goodenough, Y. Shao-Horn, *Science* **2011**, *334*, 1383.

[56] J. Xu, J. Li, D. Xiong, B. Zhang, Y. Liu, K.-H. Wu, I. Amorim, W. Li, L. Liu, *Chem. Sci.* **2018**, *9*, 3470.

[57] T. Rodenas, S. Beeg, I. Spanos, S. Neugebauer, F. Girgsdies, G. Algara-Siller, P. P. M. Schleker, P. Jakes, N. Pfaender, M. Willinger, M. Greiner, G. Prieto, R. Schloegl, S. Heumann, *Adv. Energy Mater.* **2018**, *8*, 1802404.

[58] a) C. K. Brozek, M. Dinca, *J. Am. Chem. Soc.* **2013**, *135*, 12886; b) M. Bosch, S. Yuan, W. Rutledge, H.-C. Zhou, *Acc. Chem. Res.* **2017**, *50*, 857.

[59] T. Wen, Y. Zheng, J. Zhang, K. Davey, S.-Z. Qiao, *Adv. Sci.* **2019**, *6*, 1801920.

[60] M. Liu, W. Zheng, S. Ran, S. T. Boles, L. Y. S. Lee, *Adv. Mater. Interfaces* **2018**, *5*, 1800849.

[61] a) J.-Q. Shen, P.-Q. Liao, D.-D. Zhou, C.-T. He, J.-X. Wu, W.-X. Zhang, J.-P. Zhang, X.-M. Chen, *J. Am. Chem. Soc.* **2017**, *139*, 1778; b) M. Chen, Y. Zhang, L. Xing, Y. Liao, Y. Qiu, S. Yang, W. Li, *Adv. Mater.* **2017**, *29*, 1607015; c) Y. Zhu, L. Peng, Z. Fang, C. Yan, X. Zhang, G. Yu, *Adv. Mater.* **2018**, *30*, 1706347.

[62] Y. Zhang, B. Gui, R. Chen, G. Hu, Y. Meng, D. Yuan, M. Zeller, C. Wang, *Inorg. Chem.* **2018**, *57*, 2288.

[63] Z. Xue, Y. Li, Y. Zhang, W. Geng, B. Jia, J. Tang, S. Bao, H.-P. Wang, Y. Fan, Z.-W. Wei, Z. Zhang, Z. Ke, G. Li, C.-Y. Su, *Adv. Energy Mater.* **2018**, *8*, 1801564.

[64] J.-Y. Zhao, R. Wang, S. Wang, Y.-R. Lv, H. Xu, S.-Q. Zang, *J. Mater. Chem. A* **2019**, *7*, 7389.

[65] Y. Jia, L. Zhang, A. Du, G. Gao, J. Chen, X. Yan, C. L. Brown, X. Yao, *Adv. Mater.* **2016**, *28*, 9532.

[66] Y. Lin, G. Chen, H. Wan, F. Chen, X. Liu, R. Ma, *Small* **2019**, *15*, 1900348.

[67] Y. Lin, H. Wan, D. Wu, G. Chen, N. Zhang, X. Liu, J. Li, Y. Cao, G. Qiu, R. Ma, *J. Am. Chem. Soc.* **2020**, *142*, 7317.

[68] Q. Zha, F. Yuan, G. Qin, Y. Ni, *Inorg. Chem.* **2020**, *59*, 1295.

[69] a) Y. Tang, B. L. Allen, D. R. Kauffman, A. Star, *J. Am. Chem. Soc.* **2009**, *131*, 13200; b) Z.-L. Wang, X.-F. Hao, Z. Jiang, X.-P. Sun, D. Xu, J. Wang, H.-X. Zhong, F.-L. Meng, X.-B. Zhang, *J. Am. Chem. Soc.* **2015**, *137*, 15070.

[70] X.-R. Wang, J.-Y. Liu, Z.-W. Liu, W.-C. Wang, J. Luo, X.-P. Han, X.-W. Du, S.-Z. Qiao, J. Yang, *Adv. Mater.* **2018**, *30*, 1800005.

[71] a) Z.-Q. Liu, H. Cheng, N. Li, T. Y. Ma, Y.-Z. Su, *Adv. Mater.* **2016**, *28*, 3777; b) Y. Liang, H. Wang, P. Diao, W. Chang, G. Hong, Y. Li, M. Gong, L. Xie, J. Zhou, J. Wang, T. Z. Regier, F. Wei, H. Dai, *J. Am. Chem. Soc.* **2012**, *134*, 15849.

[72] W. Chen, Y. Zhang, G. Chen, R. Huang, Y. Zhou, Y. Wu, Y. Hu, K. Ostrikov, *J. Mater. Chem. A* **2019**, *7*, 3090.

[73] B. Zhang, Z. Qi, Z. Wu, Y. H. Lui, T.-H. Kim, X. Tang, L. Zhou, W. Huang, S. Hu, *ACS Energy Lett.* **2019**, *4*, 328.

[74] Z. Zou, T. Wang, X. Zhao, W.-J. Jiang, H. Pan, D. Gao, C. Xu, *ACS Catal.* **2019**, *9*, 7356.

[75] a) A. O. Yazaydin, A. I. Benin, S. A. Faheem, P. Jakubczak, J. J. Low, R. R. Willis, R. Q. Snurr, *Chem. Mater.* **2009**, *21*, 1425; b) J.-P. Ma, S.-Q. Wang, C.-W. Zhao, Y. Yu, Y.-B. Dong, *Chem. Mater.* **2015**, *27*, 3805; c) X.-F. Lu, P.-Q. Liao, J.-W. Wang, J. X. Wu, X.-W. Chen, C.-T. He, J.-P. Zhang, G.-R. Li, X.-M. Chen, *J. Am. Chem. Soc.* **2016**, *138*, 8336.

[76] J. Zhang, X. Bai, T. Wang, W. Xiao, P. Xi, J. Wang, D. Gao, J. Wang, *Nano-Micro Lett.* **2019**, *11*, 2.

[77] X. Hu, S. Zhang, J. Sun, L. Yu, X. Qian, R. Hu, Y. Wang, H. Zhao, J. Zhu, *Nano Energy* **2019**, *56*, 109.

[78] M. Lu, Y. Li, P. He, J. Cong, D. Chen, J. Wang, Y. Wu, H. Xu, J. Gao, J. Yao, *J. Solid State Chem.* **2019**, *272*, 32.

[79] C.-P. Wang, H.-Y. Liu, G. Bian, X. Gao, S. Zhao, Y. Kang, J. Zhu, X.-H. Bu, *Small* **2019**, *15*, 1906086.

[80] F. Razmjooei, K. P. Singh, D.-S. Yang, W. Cui, Y. H. Jang, J.-S. Yu, *ACS Catal.* **2017**, *7*, 2381.

[81] Y. Li, W. Zhou, J. Dong, Y. Luo, P. An, J. Liu, X. Wu, G. Xu, H. Zhang, J. Zhang, *Nanoscale* **2018**, *10*, 2649.

[82] K. Gong, F. Du, Z. Xia, M. Durstock, L. Dai, *Science* **2009**, *323*, 760.

[83] a) J. Lee, H. Lee, B. Lim, *J. Ind. Eng. Chem.* **2018**, *58*, 100; b) M. Grden, M. Alsabet, G. Jerkiewicz, *ACS Appl. Mater. Interfaces* **2012**, *4*, 3012.

[84] H. Jia, Y. Yao, J. Zhao, Y. Gao, Z. Luo, P. Du, *J. Mater. Chem. A* **2018**, *6*, 1188.

[85] S. Aralekallu, V. A. Sajjan, M. Palanna, K. C. P. Prabhu, M. Hojamberdiev, L. K. Sannegowda, *J. Power Sources* **2020**, *449*, 227516.

[86] a) D. K. Dogutan, R. McGuire, Jr., D. G. Nocera, *J. Am. Chem. Soc.* **2011**, *133*, 9178; b) H. Jia, Z. Sun, D. Jiang, P. Du, *Chem. Mater.* **2015**, *27*, 4586.

[87] M. Gao, W. Sheng, Z. Zhuang, Q. Fang, S. Gu, J. Jiang, Y. Yan, *J. Am. Chem. Soc.* **2014**, *136*, 7077.

[88] F. Cao, M. Zhao, Y. Yu, B. Chen, Y. Huang, J. Yang, X. Cao, Q. Lu, X. Zhang, Z. Zhang, C. Tan, H. Zhang, *J. Am. Chem. Soc.* **2016**, *138*, 6924.

[89] M. Zhai, F. Wang, H. Du, *ACS Appl. Mater. Interfaces* **2017**, *9*, 40171.

[90] J. Meng, J. Zhou, H. Chi, K. Li, J. Wan, Z. Hu, *Chemistryselect* **2019**, *4*, 8661.

[91] J. Zhang, L. Yu, Y. Chen, X. F. Lu, S. Gao, X. W. Lou, *Adv. Mater.* **2020**, *32*, 1906432.

[92] H. Xu, C. Shan, X. Wu, M. Sun, B. Huang, Y. Tang, C.-H. Yan, *Energy Environ. Sci.* **2020**, *13*, 2949.

[93] a) Z. Li, M. Shao, L. Zhou, R. Zhang, C. Zhang, M. Wei, D. G. Evans, X. Duan, *Adv. Mater.* **2016**, *28*, 2337; b) C. Zhu, H. Li, S. Fu, D. Du, Y. Lin, *Chem. Soc. Rev.* **2016**, *45*, 517.

[94] a) A. Kulkarni, S. Siahrostami, A. Patel, J. K. Norskov, *Chem. Rev.* **2018**, *118*, 2302; b) W. Xia, A. Mahmood, Z. Liang, R. Zou, S. Guo, *Angew. Chem., Int. Ed.* **2016**, *55*, 2650.

[95] a) Y. Nie, L. Li, Z. Wei, *Chem. Soc. Rev.* **2015**, *44*, 2168; b) X. F. Lu, B. Y. Xia, S.-Q. Zang, X. W. Lou, *Angew. Chem., Int. Ed.* **2019**, *132*, 1910309.

[96] a) Y. Xu, Z. Huang, B. Wang, Z. Liang, C. Zhang, Y. Wang, W. Zhang, H. Zheng, R. Cao, *Chem. Commun.* **2019**, *55*, 14805; b) L. Jiao, H.-L. Jiang, *Chem* **2019**, *5*, 786; c) X. Zhang, F. Yan, S. Zhang, H. Yuan, C. Zhu, X. Zhang, Y. Chen, *ACS Appl. Mater. Interfaces* **2018**, *10*, 24920; d) W. Zhang, W. Lai, R. Cao, *Chem. Rev.* **2017**, *117*, 3717.

[97] a) M. Shao, Q. Chang, J.-P. Dodelet, R. Chenitz, *Chem. Rev.* **2016**, *116*, 3594; b) G.-L. Li, C. D. Liu, L.-F. Yuan, Q.-M. Wu, W.-W. Chen, G.-C. Cheng, B.-B. Yang, C. Hao, *Int. J. Hydrogen Energy* **2018**, *43*, 1386.

[98] a) H.-S. Lu, H. Zhang, R. Liu, X. Zhang, H. Zhao, G. Wang, *Appl. Surf. Sci.* **2017**, *392*, 402; b) M. Zhou, H.-L. Wang, S. Guo, *Chem. Soc. Rev.* **2016**, *45*, 1273.

[99] L. Huang, X. Zhang, Y. Han, Q. Wang, Y. Fang, S. Dong, *J. Mater. Chem. A* **2017**, *5*, 18610.

[100] W. Xia, J. Tang, J. Li, S. Zhang, K. C. W. Wu, J. He, Y. Yamauchi, *Angew. Chem., Int. Ed.* **2019**, *58*, 13354.

[101] a) B. Liu, H. Shioyama, T. Akita, Q. Xu, *J. Am. Chem. Soc.* **2008**, *130*, 5390; b) Y. V. Kaneti, S. Dutta, M. S. A. Hossain, M. J. A. Shiddiky, K.-L. Tung, F.-K. Shieh, C.-K. Tsung, K. C. W. Wu, Y. Yamauchi, *Adv. Mater.* **2017**, *29*, 1700213; c) R. R. Salunkhe, Y. V. Kaneti, Y. Yamauchi, *ACS Nano* **2017**, *11*, 5293.

[102] Z. Xia, J. Fang, X. Zhang, L. Fan, A. J. Barlow, T. Lin, S. Wang, G. G. Wallace, G. Sun, X. Wang, *Appl. Catal., B* **2019**, *245*, 389.

[103] S. Guo, P. Yuan, J. Zhang, P. Jin, H. Sun, K. Lei, X. Pang, Q. Xu, F. Cheng, *Chem. Commun.* **2017**, *53*, 9862.

[104] Q. Lai, Y. Zhao, Y. Liang, J. He, J. Chen, *Adv. Funct. Mater.* **2016**, *26*, 8334.

[105] a) W. Zhang, Z.-Y. Wu, H.-L. Jiang, S.-H. Yu, *J. Am. Chem. Soc.* **2014**, *136*, 14385; b) Y.-Z. Chen, C. Wang, Z.-Y. Wu, Y. Xiong, Q. Xu, S.-H. Yu, H.-L. Jiang, *Adv. Mater.* **2015**, *27*, 5010; c) B. Y. Xia, Y. Yan, N. Li, H. B. Wu, X. W. Lou, X. Wang, *Nat. Energy* **2016**, *1*, 15006.

[106] R. Chen, J. Yao, Q. Gu, S. Smeets, C. Baerlocher, H. Gu, D. Zhu, W. Morris, O. M. Yaghi, H. Wang, *Chem. Commun.* **2013**, *49*, 9500.

[107] a) C. Guan, X. Liu, W. Ren, X. Li, C. Cheng, J. Wang, *Adv. Energy Mater.* **2017**, *7*, 1602391; b) B. Motevalli, N. Taherifar, H. Wang, J. Z. Liu, *J. Phys. Chem. C* **2017**, *121*, 2221; c) H. Liang, X. Jiao, C. Li, D. Chen, *J. Mater. Chem. A* **2018**, *6*, 334.

[108] a) N. L. Torad, R. R. Salunkhe, Y. Li, H. Hamoudi, M. Imura, Y. Sakka, C.-C. Hu, Y. Yamauchi, *Chem. - Eur. J.* **2014**, *20*, 7895; b) J. Xiang, J. Li, X. Zhang, Q. Ye, J. Xu, X. Shen, *J. Mater. Chem. A* **2014**, *2*, 16905; c) Q. Lai, J. Zhu, Y. Zhao, Y. Liang, J. He, J. Chen, *Small* **2017**, *13*, 1700740; d) S. S. A. Shah, L. Peng, T. Najam, C. Cheng, G. Wu, Y. Nie, W. Ding, X. Qi, S. Chen, Z. Wei, *Electrochim. Acta* **2017**, *251*, 498.

[109] a) C. Zhu, Q. Shi, B. Z. Xu, S. Fu, G. Wan, C. Yang, S. Yao, J. Song, H. Zhou, D. Du, S. P. Beckman, D. Su, Y. Lin, *Adv. Energy Mater.* **2018**, *8*, 1801956; b) J. Wang, Z. Huang, W. Liu, C. Chang, H. Tang, Z. Li, W. Chen, C. Jia, T. Yao, S. Wei, Y. Wu, Y. Lie, *J. Am. Chem. Soc.* **2017**, *139*, 17281.

[110] K. Zhao, S. Liu, G. Ye, X. Wei, Y. Su, W. Zhu, Z. Zhou, Z. He, *ChemSusChem* **2020**, *13*, 1556.

[111] K. Zhao, S. Liu, G. Ye, Q. Gan, Z. Zhou, Z. He, *J. Mater. Chem. A* **2018**, *6*, 2166.

[112] W. Zhu, K. Zhao, S. Liu, M. Liu, F. Peng, P. An, B. Qin, H. Zhou, H. Li, Z. He, *J. Energy Chem.* **2019**, *37*, 176.

[113] R. Jasinski, *Nature* **1964**, *201*, 1212.

[114] H. Zhong, K. H. Ly, M. Wang, Y. Krupskaya, X. Han, J. Zhang, J. Zhang, V. Kataev, B. Buechner, I. M. Weidinger, S. Kaskel, P. Liu, M. Chen, R. Dong, X. Feng, *Angew. Chem., Int. Ed.* **2019**, *58*, 10677.

[115] a) J. Suntivich, H. A. Gasteiger, N. Yabuuchi, H. Nakanishi, J. B. Goodenough, Y. Shao-Horn, *Nat. Chem.* **2011**, *3*, 546; b) Y. Jiao, Y. Zheng, M. Jaroniec, S. Z. Qiao, *J. Am. Chem. Soc.* **2014**, *136*, 4394; c) Y. He, S. Hwang, D. A. Cullen, M. A. Uddin, L. Langhorst, B. Li, S. Karakalos, A. J. Kropf, E. C. Wegener, J. Sokolowski, M. Chen, D. Myers, D. Su, K. L. More, G. Wang, S. Litster, G. Wu, *Energy Environ. Sci.* **2019**, *12*, 250.

[116] T. Ling, D.-Y. Yan, Y. Jiao, H. Wang, Y. Zheng, X. Zheng, J. Mao, X.-W. Du, Z. Hu, M. Jaroniec, S.-Z. Qiao, *Nat. Commun.* **2016**, *7*, 12876.

[117] Y. Wen, H. Rong, T. Zhan, *J. Electroanal. Chem.* **2019**, *833*, 454.

[118] a) Z. Lu, W. Xu, J. Ma, Y. Li, X. Sun, L. Jiang, *Adv. Mater.* **2016**, *28*, 7155; b) Z. W. Seh, J. Kibsgaard, C. F. Dickens, I. B. Chorkendorff, J. K. Norskov, T. F. Jaramillo, *Science* **2017**, *355*, eaad4998.

[119] W. He, H.-M. Guo, R. Shimoni, Z.-Y. Lu, I. Hod, *ACS Appl. Energy Mater.* **2019**, *2*, 2138.

[120] H. Huang, S. Zhou, C. Yu, H. Huang, J. Zhao, L. Dai, J. Qiu, *Energy Environ. Sci.* **2020**, *13*, 545.

[121] a) X. Lv, J. Rao, Y. Wang, Y. Liu, Z.-Y. Yuan, *ACS Sustainable Chem. Eng.* **2019**, *7*, 8993. b) Q. Wang, Z. Zhang, X. Zhao, J. Xiao, D. Manoj, F. Wei, F. Xiao, H. Wang, S. Wang, *ChemElectroChem*, **2020**, *7*, 289.

**ADVANCED
SCIENCE NEWS**

www.advancedsciencenews.com

**ADVANCED
ENERGY & SUSTAINABILITY
RESEARCH**
Open Access

www.advenergysustres.com

[122] J. Shi, F. Qiu, W. Yuan, M. Guo, Z.-H. Lu, *Chem. Eng. J.*, **2021**, *403*, 126312.

[123] Z. Gao, Z. W. Yu, F. Q. Liu, Y. Yu, X. M. Su, L. Wang, Z. Z. Xu, Y. L. Yang, G. R. Wu, X. F. Feng, F. Luo, *Inorg. Chem.* **2019**, *58*, 11500.

[124] W.-J. Dang, Y.-Q. Shen, M. Lin, H. Jiao, L. Xu, Z.-L. Wang, *J. Alloys Compd.* **2019**, *792*, 69.

[125] Z. Xue, K. Liu, Q. Liu, Y. Li, M. Li, C.-Y. Su, N. Ogiwara, H. Kobayashi, H. Kitagawa, M. Liu, G. Li, *Nat. Commun.* **2019**, *10*, 5048.

[126] J. Li, W. Xia, J. Tang, H. Tan, J. Wang, Y. V. Kaneti, Y. Bando, T. Wang, J. He, Y. Yamauchi, *Nanoscale Horiz.* **2019**, *4*, 1006.

[127] W. Xia, R. Zou, L. An, D. Xia, S. Guo, *Energy Environ. Sci.* **2015**, *8*, 568.

Jue Hu received her Ph.D. from the Chinese Academy of Sciences and conducted her postdoctoral training from Brookhaven National Laboratory (US) and Hong Kong University of Science and Technology. She currently works as a professor at Kunming University of Science and Technology. Her research interests are rational design and synthesis of functional materials for electrocatalysis applications.

Bolong Huang received his Ph.D. in 2012 from the University of Cambridge, and his B.Sc. in Condensed Matter Physics from the Department of Physics, Peking University, 2007. Following a systematic training period as a research assistant at Peking University, and in Hong Kong, he started his independent research as PI in the Hong Kong Polytechnic University in 2015. His main research fields are density functional theory (DFT) calculations on rare earth functional nanomaterials, defect theory of solid functional nanomaterials, DFT calculation development based on ab initio electronic self-energy corrections, and semi-core orbital corrections as an implement in time-dependent DFT theory.

Chengxu Zhang received his Ph.D. from University of Science and Technology of China (USTC) in 2012. He currently works as associate professor at Kunming University of Science and Technology. He is interested in developing and fabricating efficient photocatalysts and electrocatalysts for electrochemical energy conversion.